Histochem Cell Biol (2010) 133:375–404
DOI 10.1007/s00418-010-0676-z

ORIGINAL PAPER

Albumin-based nanoparticles as magnetic resonance contrast agents: I. Concept, first syntheses and characterisation

M. M. Stollenwerk · I. Pashkunova-Martic · C. Kremser · H. Talasz · G. C. Thurner · A. A. Abdelmoez · E. A. Wallnöfer · A. Helbok · E. Neuhauser · N. Klammsteiner · L. Klimaschewski · E. von Guggenberg · E. Fröhlich · B. Keppler · W. Jaschke · P. Debbage

Accepted: 21 January 2010 / Published online: 20 February 2010

Abstract To develop a platform for molecular magnetic resonance imaging, we prepared gadolinium-bearing albumin-polylactic acid nanoparticles in the size range 20–40 nm diameter. Iterative cycles of design and testing upscaled the synthesis procedures to gram amounts for physicochemical characterisation and for pharmacokinetic testing. Morphological analyses showed that the nanoparticles were spheroidal with rough surfaces. Particle sizes were measured by direct transmission electron microscopical measurements from negatively contrasted preparations, and by use of photon correlation spectroscopy; the two methods each documented nanoparticle sizes less than 100 nm and generally 10–40 nm diameter, though with significant intrabatch and interbatch variability. The particles' charge sufficed to hold them in suspension. HSA retained its tertiary structure in the particles. The nanoparticles were stable against turbulent flow conditions and against heat, though not against detergents. MRI imaging of liquid columns was possible at nanoparticle concentrations below 10 mg/ml. The particles were non-cytotoxic, non-thrombogenic and non-immunogenic in a range of assay systems developed for toxicity testing of nanoparticles. They were micellar prior to lyophilisation, but loosely structured aggregated masses after lyophilisation and subsequent resuspension. These nanoparticles provide a platform for further development, based on non-toxic materials of low immunogenicity already in clinical use,

Electronic supplementary material The online version of this article (doi:10.1007/s00418-010-0676-z) contains supplementary material, which is available to authorized users.

M. M. Stollenwerk
Faculty of Health and Society, Malmö University,
205 06 Malmö, Sweden

I. Pashkunova-Martic · B. Keppler
Institute of Inorganic Chemistry, University of Vienna,
Währinger Str. 42, 1090 Vienna, Austria

C. Kremser · G. C. Thurner · E. A. Wallnöfer · W. Jaschke
Department of Radiology, Innsbruck Medical University,
Anichstrasse 35, 6020 Innsbruck, Austria

H. Talasz
Section for Clinical Biochemistry,
Biozentrum of the Medical University Innsbruck,
Fritz-Pregl-Straße 3, 6020 Innsbruck, Austria

A. A. Abdelmoez · E. Neuhauser · N. Klammsteiner · P. Debbage (✉)
Department of Anatomy, Histology and Embryology,
Innsbruck Medical University, Müllerstrasse 59,
6020 Innsbruck, Austria
e-mail: Paul.Debbage@i-med.ac.at

A. Helbok · E. von Guggenberg
Department of Nuclear Medicine, Innsbruck Medical University,
Anichstrasse 35, 6020 Innsbruck, Austria

E. Fröhlich
Center for Medical Research, Stiftingtalstrasse 24,
8010 Graz, Austria

Present Address:
A. A. Abdelmoez
Department of Pharmaceutical Organic Chemistry,
Assiut University, Assiut, Egypt

L. Klimaschewski
Division of Neuroanatomy, Department of Anatomy,
Histology and Embryology, Innsbruck Medical University,
Müllerstrasse 59, 6020 Innsbruck, Austria

not expensive, and synthesized using methods which can be upscaled for industrial production.

Keywords Human serum albumin · Nanoparticles · MRI · Contrast medium · Chelate · Gadolinium

Introduction

Molecular imaging, like histochemistry, generates speci c contrast in speci ed tissue elements and therefore, like histopathology, has wide potential clinical application, with the advantage of being minimally invasive. It uses a range of imaging modalities and one of these, diagnostic molecular imaging in the form of nuclear medicine, already has an established role in clinical practice. Nuclear imaging allows the detection of molecular probes with high sensitivity and provides high-contrast images, but with limited spatial resolution. Other imaging modalities, which use non-ionising signal emission, such as magnetic resonance imaging, provide higher spatial resolution, but involve detection of weak radio signals and so show much lower sensitivity. New reagents in the form of nanoparticles are necessary to act as signal ampli ers (Debbage and Jaschke 2008), and their use allows molecular imaging to be carried out by use of magnetic resonance tomographic imaging (MRI) (Anderson et al. 2000; Flacke et al. 2001; Hauff et al. 2004; Johansson et al. 2001; Kang et al. 2002; King et al. 2002; Laurent et al. 2004; Paschkunova-Martic et al. 2005; Sipkins et al. 1998; Winter et al. 2003) or by optical imaging (Lewis et al. 2006), for comprehensive reviews see (Debbage and Jaschke 2008; Preda et al. 2006; Torchilin 2002). The nanoparticle is the basic platform for molecular imaging in non-ionising modalities. However, designing particles for molecular imaging poses a series of signi cant challenges. Now that proof of principle has been achieved in many laboratories, the next step is to design practicable agents for research and clinical applications. Nanoparticles for industrial fabrication and use as pharmaceutical agents must be safe and ef cient and highly standardised. Until now, these challenges have been met for only a single class of nano-agents for use in diagnostic imaging, the ultrasmall particles of iron oxide (USPIOs: Daldrup-Link and Brasch 2003; Enochs et al. 1999; Preda et al. 2006; Seneterre et al. 1996; Singh et al. 2008). USPIOs cause a focal signal drop on T2/T2* weighted images. The area of signal drop is much larger than the area of USPIO accumulation. This "glooming" effect of USPIOs renders quanti cation and exact localisation dif cult. In addition, USPIOs may go undetected if they are located close to structures with signal void such as the air lled bowel lumen or vascular structures. Thus, the development of a nanoparticular signal enhancer resulting in an ampli cation of a positive contrast is of great interest. Furthermore, the development of nanoparticles delivering positive contrast promises a number of advantages, including targeting of high concentrations of contrast medium exclusively to a single site, achieving extremely high densities of signal-enhancing materials due to their attachment on nanoparticles, and coupling signal generation to drug delivery.

For non-metal-based particles, most of the principles which will govern their design remain to be elucidated. A few principles have become familiar, for example, that single macromolecules (less than 10 nm diameter) are too small to provide adequate signal strengths in non-ionising imaging modalities, because the signal-group loading is inadequate or because signal-group overloading tends to disrupt molecular function (Andersen-Berg et al. 1986; Shahbazi-Gahrouei et al. 2001, 2006; Shapiro et al. 2006; Unger et al. 1985). Similarly, drug overloading can result in loss of macromolecule function (Stehle et al. 1997); for the declared aim of combined diagnostics and therapy (theranostics) (Boisseau et al. 2006), adequately large particles must be used. As a result, nanostructures larger than 20 nm diameter are being considered for further development. Each such structure can bear several thousand agents to provide high image contrast without overloading the functional groups and yet leave space for the addition of targeting groups. A second principle is to avoid nanostructures much larger than 100 nm diameter, which may cause mechanical damage to cells *en passant* (Paschkunova-Martic et al. 2005) or which enter cells by inappropriate routes (Frank et al. 2003). Particles within the size range of most viruses (20–200 nm) are emerging as the most favoured for molecular imaging. This brings the synthetic particles into the same size range as many elements of the cellular machinery, for example, the ribosome (~30 nm diameter), the nuclear pore [~145 nm diameter, ~40 nm depth (Alber et al. 2007a, b)], the typical ion channel (4 nm pore diameter and 20 nm external diameter), DNA and RNA (2 nm diameter), several classes of intracellular vesicles (40–60 nm diameter), the various elements of the cytoskeleton in their strand thickness dimension (4, 10, 25 nm) and even the cell membranes in one of their dimensions (thickness: 10 nm). Most extracellular bres, such as collagen (60 nm diameter), and many of the matrix molecules, such as glycosaminoglycans (3 nm diameter chains of 250 nm length), are also nanostructures. The consequences of introducing synthetic nanostructures amongst the similar sized extracellular and intracellular nano-machinery cannot yet be foreseen, but it is worth noting that unfamiliar risks may wait here. To assess the possible risks, it is essential as part of design and development of diagnostic imaging nanoagents to obtain nanoparticles of well-de ned and standardised sizes. Other design principles address the quantitative relationships amongst the various functionalities of the nanostructures, for example, the minimum number of contrast-enhancing agents that must be present on the particles:

many such agents have toxic potential, as highlighted recently for gadolinium (Broome et al. 2007; Collidge et al. 2007; Cowper et al. 2000, 2007; Khurana et al. 2007; Rofsky et al. 2008; Sadowski et al. 2007). Similarly, the materials used to construct the particles must be non-toxic and non-immunogenic, ruling out the present generations of quantum dots, and also affordable for bulk fabrication (for review, see Moghimi et al. 2001). To facilitate later industrial fabrication, the laboratory synthesis selected must not be overly elaborate. To allow for future developments such as theranostics, the matrix materials should easily permit loading of the particles with drugs. It is evident that, at present, major branches of knowledge in molecular imaging stand at the very beginning of their development.

We presented earlier a proof of principle of molecular imaging in MRI (Paschkunova-Martic et al. 2005), but this was based on latex nanoparticles, which are potentially allergenic and therefore cannot be developed towards clinical applications. In order to develop nanoparticles with clinical relevance, we considered the criteria noted above and selected human albumin as matrix material for further developmental work. This protein is particularly well suited for this purpose. It has been in clinical use in critical care medicine as a hypovolemic shock treatment since before 1950 (Colgan et al. 2000; Erstad 1996; Peters 1996; Tabor 1999; Yaxley 2009). After 1998, this use became controversial, so that the small number of adverse reactions to it has been under continuous study (Cochrane Review 1998; Finfer et al. 2004; Ring and Messmer 1977; The Albumin Reviewers 2004; Wilkes and Navickis 2001). Due to its clinical applications, the industrial preparation and logistics of albumin are well established (for example, http://www.albumintherapy.com). Recently, albumin has been used to replace the cremophore oil component used in taxane formulations such as taxol, used in chemotherapy in oncological applications. The taxane core is coated with albumin allowing therapeutic exploitation of at least two features of malignant tumours, namely (1) enhanced permeability and (2) retention and the enhanced expression of SPARC receptors. This formulation, “Abraxane”, eliminates the requirements for special tubing and for corticosteroid premedication during application of chemotherapy. Abraxane is better tolerated by the patient, allowing 33% more taxane to be delivered to the tumour and raising clinical response rate by almost two times; the better response rate obtained in metastatic breast cancer has made this nanoparticle formulation into a blockbuster drug. Albumin is abundantly available, in that human plasma contains approximately 45 g/l (He and Carter 1992), representing 50–60% of total plasma protein. It is not expensive and can be produced in exceptionally high yields (g/l) by recombinant expression (Cregg et al. 2000), the recombinant form exhibiting safety and efficacy in clinical trials (Chuang and Otagiri 2007). Its gene sequence and aminoacid sequence, of 585 residues with 17 pairs of disulfide bridges and one free cysteine (Behrens et al. 1975; Brown 1975; Dugiaczyk et al. 1982; Peterson and Foster 1965; Meloun et al. 1975) have long been known, and its three-dimensional structure has been elucidated at 2.8 Å (Carter and Ho 1994; Curry et al. 1998; He and Carter 1992; Ho et al. 1993) and 2.5 Å (Sugio et al. 1999) resolution in the native form, and also in the presence of bound fatty acids (Curry et al. 1999). It is understood how unique and highly flexible multiple double bridges formed by disulfide bonds unite to form two major ligand-binding sites within subdomains of the molecule (Peters 1977; Sugio et al. 1999); its secondary and its tertiary conformation have been investigated by infrared and Raman spectroscopy (Ivanov et al. 2002). Its physiological roles in regulating blood volume and transporting molecules have been carefully researched (Fehske et al. 1981; Goldwasser and Feldman 1997; Gonzalez and Kannewurf 1998; Griffel and Kaufman 1992; Kragh-Hansen 1981; Peters 1985; Putnam 1984; Rainey and Read 1994). This well studied molecule, with its long history of clinical use, is a good candidate for use in imaging work. It satisfies the several design criteria posited above, and several research groups have used it as the basis for MRI contrast agents. One MRI contrast agent presently in clinical use bases upon temporary attachment of modified gadolinium chelates to albumin in the bloodstream in order to obtain contrast amplification for blood-pool imaging (Farooki et al. 2004; Lauffer et al. 1998; Parmelee et al. 1997). Its use as a carrier for covalently bound gadolinium chelates in MRI has been documented in a long series of reports (summarised in Daldrup-Link and Brasch 2003; Schmiedl et al. 1987). The potential advantages but also the potential risks of albumin-based compounds have therefore been investigated, providing a solid base of research evidence that can be used to construct optimised nanoparticles. Numerous studies have shown that albumin can be formed into nanoparticles and microparticles by several methods. It can be aggregated to do so (Baranov et al. 2004). It can be desolved (Langer et al. 2003; Marty et al. 1978; Vogel et al. 2002; Weber et al. 2000a, b) and co-acervated to do so (Langer et al. 2003; Lin et al. 1993; Merodio et al. (2001); Weber et al. 2000a, b). It can be formed into microstructures by emulsification with polymers (Gallo et al. 1984; Müller et al. 1996) such as polylactic acid (PLA) (Montisci et al. 2001). Several authors have applied albumin as a coating for PLA nanostructures (Brazile et al. 1992; Verrecchia et al. 1993) and for taxanes. PLA offers excellent biocompatibility and biodegradability, and has been used extensively to form carriers for drug delivery (Blanco-Prieto et al. 2004). In summary, a solid technological basis exists upon which further development can build (Moghimi et al. 2001; Riess 2003).

Our work therefore examined the synthesis and standardisation of human albumin-PLA (HSA-PLA) nanoparticles for

use in MRI, con rming and characterising their properties as signal-emitting nanoparticles. To do this, we attached gadolinium to the HSA in the form of DTPA–gadolinium (DTPA–Gd) chelates (Fig. 1). Gd is a well-established signal enhancer in MRI, giving a bright signal on T1 weighted images. Quanti cation is possible and Gd does not give rise to signal "glooming". We selected DTPA as chelator for this initial series of batches, although we were aware of the signi cantly greater stability of DOTA and other macrocyclic chelators. Part of the reason for this selection was that macrocyclic chelators require more complex chemistry to conjugate them to the protein and they are also signi cantly more expensive. Furthermore, this initial development of albumin-based nanoparticles retained DTPA from our earlier proof of principle work (Paschku-nova-Martic et al. 2005). This manuscript aims to move on from proof of principle to develop nanoparticles which can be developed in a translational fashion for use in clinical applications. This makes it necessary to construct nanoparticles which are safe and ef cient for application in humans, an aspect which we address here in connection with the basic model of the nanoparticle. A preliminary requirement was to synthesize nanoparticles which are stable in body uids for suf cient time to allow imaging. Since nanoparticles are complex structures, there were different types of stability to be considered. The rst of these was the internal cohesion of the entire particle, which should ensure that it retains its integrity in body uids and does not disintegrate into its components; this type of stability we termed "structural integrity". A second type of stability concerned the retention of the contrast-enhancing metal (gadolinium, Gd) in its chelated form within the nanoparticle. Leakage of this toxic metal out of the nanoparticles must be minimised. This second type of stability we termed "chelate stability". A second requirement is to determine and to regulate the size of nanoparticles, which is of critical importance for their function and biology (Barratt 2000; Yuan 1998); one important criterion for success is the degree to which particle size and dispersity can be standardised. As major determinant of drug-delivery capacity and of targeting-group density, the number of albumin molecules comprising each nanoparticle is an important correlate of the size and a primary parameter describing the nanoparticles (Debbage 2009). Two other parameters are co-determinants: the protein density and the albumin molecule packing density within the nanoparticle; a prime aim of particle characterisation is to assign maximally precise values to these three parameters.

This initial exploration dispensed with elaboration: we did not provide our nanoparticles with stealth properties by PEGylation, nor did we attach targeting groups to the particles, or load them with speci c ligands. We focussed instead on examining the physicochemical properties of albumin-based nanoparticles produced by iterative use of a protocol which was carefully standardised. To develop this protocol, we found it necessary to work through two cycles of iterative design, development and characterisation, this report re ects this process. Later papers in this series will address further

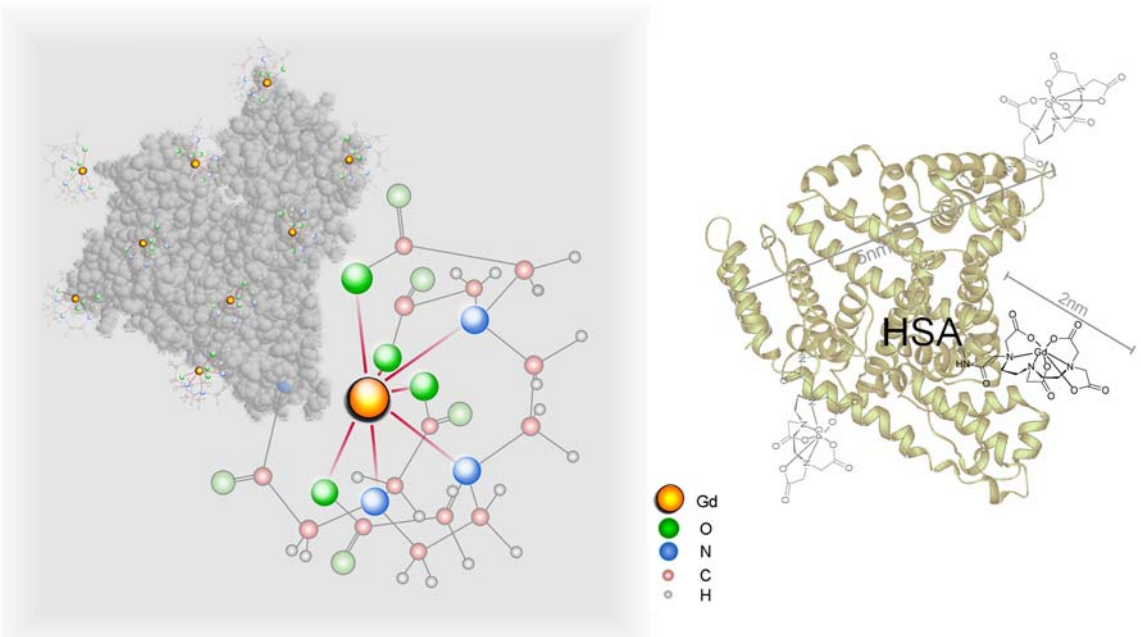

Fig. 1 At *left*, a conceptual sketch showing the structure of the DTPA–Gd chelate, which is attached to an albumin molecule (background). The albumin molecule shown here bears 10 DTPA chelates. At *right*, the structure of the albumin molecule together with size details and with DTPAGd chelates attached

standardisation of the nanoparticles, and their elaboration as multifunctional agents designed for clinical applications.

Materials and methods

Materials

Poly (DL-lactic acid) (PLA), human serum albumin (HSA) Fraction V, rat serum albumin, citric acid monohydrate, sodium citrate tribasic dihydrate, sodium hydroxide, dimethylsulfoxide (DMSO), nitrilotriacetic acid trisodium salt ($Na_3C_6H_6NO_6$) (Na_3NTA), diethylenetriaminopentaacetic acid bisanhydride (DTPABA), HEPES crystals and sodium azide were purchased from Sigma-Aldrich (Munich, Germany). Gadolinium oxide, Gd_2O_3, 99% was a gift from Dr. Peter Unfried, Institute of Inorganic Chemistry at the University of Vienna. Glutaraldehyde 25% (EM grade) was obtained from Merck (Darmstadt, Germany), cacodylate buffer from Serva (Heidelberg, Germany), osmium tetroxide, copper and nickel grids (150 mesh), and Formvar were from Gröpl (Tulln, Austria); reagents needed for Epon were from Serva. Throughout this work, the water used was purified Millipore water (Millipore, Billerica, MA, USA). Materials for PAGE, including the gels, the running and the sample buffers, and the standards, were obtained from BioRad (Vienna, Austria).

Purification and extraction procedures

The purpose of this developmental work was to design protocols capable of synthesising gram amounts of nanoparticles. In an iterative design and testing procedure, nanoparticles were synthesised, characterised and tested, and any flaws noted. A new cycle of design and synthesis then eliminated the flaws, and was tested in its turn. The interplay of the several, various design requirements is shown in this paper by comparing these batches. At each step of development, the synthesis protocol was standardised for that step.

Size exclusion chromatography (fast protein liquid chromatography, FPLC)

FPLC was used in *series I* to purify the reaction product after each derivatisation step. The reaction mixture was purified by passage through two gel filtration columns (each of 5 ml volume), applied sample volume 0.5 ml, flow rate 0.6 ml/min, size exclusion matrix of Sephadex G-25 superfine (Amersham Biotech) against citrate buffer (100 mM, pH 6.5). The separations were performed with a chromatography system ÄKTA purifier 10 (Amersham Pharmacia Biotech). The batch sizes were 10–50 mg, too small by a factor of 50× for adequate characterisation and testing.

Dialysis

In *series II*, dialysis was used to purify the reaction product after each derivatisation step. Membranes with cut-off of 12–14, 100 and 500 kDa were used.

Preparation and characterisation of the HSA–DTPA–Gd conjugates

Conjugation of DTPABA to HSA

To prepare a single batch of nanoparticles in *series II*, approximately 5 g of HSA-DTPA conjugate were synthesised. HSA (5.00 g, $7.5e^{-05}$ M) was dissolved in 200 ml HEPES buffer (100 mM, pH 8.8). A 220-fold excess of DTPABA (5.86 g, $1.64e^{-02}$ M) was suspended in 17.5 ml DMSO and added portion-wise to the protein solution. After each portion, the pH was adjusted to 8.5 (*series I*) or 8.8 (*series II*) by means of 3 M NaOH, then the reaction mixture was stirred for 2 h at RT. Dialysis was carried out in citrate buffer (0.1 M, pH 6.5) (*series I*), in water through a membrane with 12,400 Da cut-off and four times solvent exchange (*series II*). In *series II*, the conjugate was lyophilised. The resulting HSA–DTPA conjugates were ready for chelation of metals, in this investigation gadolinium (Gd) or radioactive indium (^{111}In).

Preparation of trisodium bis(nitrilotriacetate), (NTA) gadolinate $Na_3Gd(NTA)_2$

The method used was similar to that described by Cooper et al. (2006) and by Paschkunova-Martic et al. (2005), starting with gadolinium oxide:

$$Gd_2O_3 + 6\ HCl \rightarrow 2\ GdCl_3 + 3\ H_2O;$$

$$GdCl_3 + 2\ Na_3NTA \rightarrow Gd(NTA)_2Na_3 + 3\ NaCl$$

Gadolinium oxide (2.10 g, $5.8e^{-03}$ M) was suspended in 3.43 g of 37% HCl solution ($9.4e^{-02}$ M), the suspension heated to boiling and further HCl added drop-wise until the solution cleared. After cooling to 40°C, the reaction mixture was diluted with distilled water to 60 ml, trisodium bis(nitrilotriacetate) (6.38 g, $2.32e^{-02}$ M) was added, the pH adjusted to 6.0 with 3 M NaOH, and the solution made up to 100 ml with distilled water.

Gadolinium complexation to HSA-DTPA

The principle of this chelation is shown in Fig. 1. 10.5 ml $Na_3[Gd(NTA)_2]$ solution (116 mM, pH 6.0) was added to 5 g HSA–DTPA in 200 ml citrate buffer giving a

$Na_3[Gd(NTA)_2]$ molar excess of 16, and the mixture stirred for 24 h at 4C. Following dialysis for 24 h against water with a cut-off MW 12,400, the chelated conjugate was lyophilised.

Preparation and characterisation of the nanoparticles

As noted above, two series of nanoparticle batches were prepared with slightly different protocols, and will be denoted as *series I–II*. The synthesis protocol based upon methods described by Montisci et al. (2001). Poly(DL-lactic acid), PLA, with molecular mass nominally 90 kDa (but in fact 70–120 kDa) was used as obtained; 7.2 ml PLA 10% w/v in methylene dichloride (*series II*: 10 ml) was added dropwise to 500 ml albumin–gadolinium conjugate (2% w/v solution in water), giving a ~1:10 w/w proportion of PLA:HSA. The mixture was emulsi ed in 100 ml aliquots each for 10 min (*series II*: 3 min) at 20,000 or 24,000 rpm by means of an IKA-Werke DI 25 basic dispergator (Janke and Kunkel KG, Staufen, Germany). Subsequently, the emulsion was stirred over night at room temperature (*series II*: 2 h). In *series I*, the emulsions were then puri ed by centrifugation at 3,324 *g* for 15 min, and both pellet and supernatant were collected and examined. After this, pellets were suspended in water and then lyophilised. In some batches of *series II*, the nanoparticle emulsions were passed through paper lters to remove excess PLA. In all batches, the emulsions were then dialysed against water (cut-off at 100 kDa), then frozen in liquid nitrogen and nally lyophilised (at −52 C and 58×10^{-3} Megabars).

Radiolabelling of the nanoparticles with Indium-111

HSA-DTPA/PLA nanoparticles, containing albumin-DTPA conjugates but without chelated Gd, were used for radiolabelling. 20–200 MBq $^{111}InCl_3$ (Perkin Elmer, Shelton, CT, USA) in 0.05 M HCl (Biochemical grade, FLUKA, Switzerland) and 0.04–0.10 ml sodium acetate (0.67 M)/2,5-dihydroxybenzoic-acid (0.24 M) buffer, with pH adjusted to 5, were added to the nanoparticles suspended in water (0.025–5 mg/ml), resulting in a total volume of 0.2 ml, followed by incubation of the reaction mixture at room temperature for 30 min. Labelling ef ciency (radiochemical yield>95%) was determined by instant thin layer chromatography on silica gel strips (Pall cooperation, East Hills, NY, USA) using two different mobile phases. System 1: 0.1 M sodium citrate pH 5; retention factor (Rf) ("free" radionuclide)= 0.8–1.0, Rf (radiolabelled nanoparticles and radiocolloid)= 0.0–0.3. System 2: pyridine/acetic acid/H_2O (3/5/1.5, v/v/v); Rf (radiocolloid)= 0.0–0.2, Rf (radiolabelled nanoparticles and "free radionuclide")= 0.8–1.0. Radioactivity distribution was analysed by electronic autoradiography (Cyclone Plus Phosphor Imager, PerkinElmer, Waltham, USA).

Physicochemical characterisation: analytical techniques

Polyacrylamide gel electrophoresis (PAGE)

PAGE in the presence of SDS (SDS-PAGE) was used to estimate the average molecular weight of HSA and of HSA–DTPA–Gd, by comparison with molecular-weight standards (Lactan, Graz, Austria). Electrophoresis using a 5 or 7.5% stacking gel and a 15% separating gel was performed in a Mini Protean II slab gel unit (Bio-Rad Laboratories, USA). Gels were stained with Coomassie blue, destained by diffusion and dried. The ratio of DTPA bound to HSA was estimated using SDS-PAGE of samples from each step during nanoparticle preparation. The method also allowed estimation of the stability of conjugate as well as of nanoparticles under exposure to the denaturation effect of SDS.

Graphite furnace atomic absorption spectrometry (AAS)

AAS was carried out to measure gadolinium concentrations as described by Liang et al. (1991) at 407.8 nm and 2,500 C atomization temperature under an argon atmosphere (Unicam 939 QZA spectrometer). The calibration solutions (1.5 μg/ml to 25 μg/ml Gd) were prepared by adequate dilution of a 1,015 μg/ml Gd atomic absorption standard solution (Sigma-Aldrich, Germany) with 0.01 % ultrapure hydrochloric acid (Merck, Germany) and high-purity water (Milli-Q system, Millipore).

Protein content

The protein in samples of puri ed HSA–DTPA–Gd and of nanoparticles was assayed employing the methods we described earlier (Paschkunova-Martic et al. 2005). Prior to assay, samples were dialyzed to remove free citrate. UV spectrometry was carried out using Amido Black as follows: 10 ml of 0.1 g/ml Amido Black 10B dye (solution A) was dissolved in a mixture of 30 ml methanol and 70 ml 99% acetic acid; solution B (washing solution) was a mixture of 80 ml methanol and 10 ml 99% acetic acid; solution C was 1 M NaOH. The protein sample was dissolved in 1 ml of water, and 2 ml of solution A were added. The sample was cooled on ice and then vortexed intensively for 10 min. After centrifugation at 3,330 *g* for 10 min at 0 C, the supernatant was discarded, and the pellet was washed several times with solution B. Afterwards, the pellet was dried at RT. The dry mass was then re-dissolved in 3 ml of solution C, and photometrical determination carried out at $\lambda = 625$ nm. The calibration curve was made by using BSA solutions of different concentration. In some cases, the Pierce assay for proteins was used to measure the protein content of puri ed HSA–DTPA–Gd and of nanoparticles,

using bicinchoninic acid (Pierce, Rockford, USA). HSA was used as standard.

PLA concentration

To assay PLA in the nanoparticles they were treated with sodium hydroxide to hydrolyse D,L-lactic acid polymers (PLA) to free D- and L-lactic acid. The polymer was hydrolysed in a 1.0 N aqueous sodium hydroxide solution at 110 C for 20 h, resulting in production of both D- and L-lactic acid (equal amounts). The sample was diluted (1/10 or 1/5) with 0.4 M hydrazine buffer, 0.5 M glycine, pH 9.0. L-lactic acid in the resulting solution was enzymatically digested by L-lactic acid dehydrogenase at 25 for 60 min, reducing nicotinamide adenine dinucleotide (NAD) to NADH (reduced form of NAD) and oxidising L-lactic acid to pyruvate hydrazone; the concentration of L-lactic acid was then determined by an absorbance analysis of NADH at 340 nm. Because the PLA polymer is a racemic mixture of 50% D- and 50% L-lactic acid, the amount of PLA was assumed to be twice the measured amount of L-lactic acid.

Relaxivity measurements of the conjugates and nanoparticles

The MR properties were measured by employing the methods and acquisition sequences we described earlier (Paschkunova-Martic et al. 2005). Serial dilutions of the samples were prepared in distilled water. All MR measurements were performed on standard clinical 1.5 T whole body MR systems (Magnetom Avanto, Siemens, Germany) using a linear polarised small loop receive coil. T_1 measurements were performed using an inversion recovery sequence (TR = 3.6 ms, TE = 2.1 ms, flip angle = 8°, receive bandwidth = 490 Hz/pixel, FOV = 67 mm, acquisition matrix = 64 × 128, 1 slice, slice thickness = 5 mm) with 15 different inversion times ranging between 140 ms and 4,000 ms. T_2 measurements were performed using a CPMG-type multi echo spin-echo sequence (TR = 1,000 ms, TE = $n \times 13.5$ ms with $n = 1,\ldots,16$, receive bandwidth = 130 Hz/pixel, FOV = 51 mm, acquisition matrix = 128 × 128, 1 slice, slice thickness = 3 mm). T_1 and T_2 parameters were calculated by a two-parameter fit to the obtained signal intensities. Relaxivities were calculated from the obtained relaxation rates R_1 (and R_2) of the dilution series by means of linear regression.

Photon correlation spectroscopy (PCS)

To assess nanoparticle sizes, measurements were carried out using a Submicron Particle Sizer Nicomp 380 DLS (Particle Sizing Systems, Santa Barbara, CA, USA). Measurements were usually carried out in purified Millipore water. Nanoparticle concentrations were chosen to produce a measurement intensity of about 300 kHz. During measurements, the temperature was held constant at 23 °C. Each sample—both conjugates and nanoparticles before and after lyophilisation—was measured for 90 min (3 cycles, each with 30 min run time). The Nicomp DLS was calibrated using standard 92 nm latex beads (Duke Scientific, Fremont, USA) at 3-monthly intervals. Nicomp intensity weight thresholds were used below 2%, channel width was set to 10 μs, but in AUTO mode was 10–200 μs; data were collected until convergence. For $\chi^2 > 2.0$, Nicomp analyses were used, for $\chi^2 < 2.0$, Gaussian analyses were used. Fit errors near zero, and residuals near zero, signalled reliable results.

Zeta potentials

The surface charge properties of the conjugates and nanoparticles were analysed by measuring their electrophoretic mobility using a PSS NICOMP™ 380 DLS/ZLS. All measurements were carried out in purified Millipore water and at room temperature.

Negative contrast transmission electron microscopy (TEM)

Electron microscopy was employed to assess nanoparticle diameters and size variability. Nanoparticles in 0.15 of aqueous suspension (10 mg/ml) were dried down onto a formvar-coated grid, then an aqueous solution of uranyl acetate (1–3%) allowed to dry down on top of the first sample. Digital images were acquired at 100,000× magnification at a Philips CM120 electron microscope. The areas of 100–200 particles from each grid were measured. Initially, nanoparticle diameters in the images were measured by hand and the average size and the polydispersity index (PDI) calculated manually. Subsequently, nanoparticle areas were measured by use of a semi-automated procedure in the Metamorph program (Zeiss, Germany), and the data processed in a spreadsheet program, to calculate nanoparticle average volume and PDI for the image. In slight adaptation of the methodology employed in polymer chemistry, PDI was defined as the ratio of the [population average particle volume based on particle volumes] to the [population average particle volume based on particle numbers]: $\frac{\overline{V_W}}{\overline{V_N}}$. The nature of this calculation is considered further in the "Discussion", below. Several PDI values were obtained for each nanoparticle batch, based on at least 1,000 nanoparticles recorded from well-separated areas of one grid or from 2 to 3 grids. PDI relates to the normal statistical parameters (mean = n, standard deviation = σ) according to the formulae:

Coefficient of variation (CV) $= \sqrt{PDI - 1}$ and CV $= \sigma/n$

For further details, see the Supplementary Information.

Calculation of nanoparticle masses

This was carried out in two ways. The first method measured several parameters, as follows: diameter (d in nm) of the particles; conjugate density of HSA–DTPA–Gd 1.4 g/cm^3; packing density δ of albumin molecules in the nanoparticles; the value of δ lay between 0.35–0.45, and was generally entered into the calculation as 0.40. The results of the calculation were obtained first as nanoparticle mass M_g measured in grams, and this was then converted to nanoparticle mass M_{Da} expressed as Daltons:

$$M_g = \left[4/3.\pi.(d/2)^3 \times 10^{-21} \times 1.4 \times \delta\right] \text{grams}$$

$$M_{Da} = \left[M_g/1.66054e^{-24}\right] \text{Daltons}$$

Ultrastructural analyses of nanoparticles

The nanoparticle suspension was fixed in 2.5% glutaraldehyde in cacodylate buffer. For small samples, 1% osmium tetroxide was added to the suspension and the mixture incubated at room temperature for 1 h prior to centrifugation; the pellet was then dehydrated in an acetone series and embedded in Epon. During some of the embedments, thorough washing was employed to remove all remaining osmium tetroxide, prior to the dehydration sequence. For larger samples, the nanoparticles fixed in glutaraldehyde in cacodylate buffer, were pelleted by centrifugation, then rinsed in cacodylate buffer in two cycles of resuspension and pelleting; the final pellet was fixed in osmium tetroxide, dehydrated in an acetone series and embedded in Epon. Ultrathin sections were cut and viewed in a Philips CM120 electron microscope without uranyl and lead contrasting.

Assessment of packing density

Image processing In some images of nanoparticles embedded in Epon without prior osmium tetroxide postfixation, contrast was too low for examination by eye. These images were scanned to produce 8-bit digital images, then relevant regions of the greyscale spectrum were assigned false colours to generate high contrast images, using methods similar to those we described earlier (Soelder et al. 2009). The false colours depicted more electron-dense (red), less electron-dense (orange), minimally electron-dense (yellow) and electron density identical with "empty" Epon (green). By thresholding the greyscale image and acquiring histograms quantifying relative areas of the image showing selected regions of the greyscale spectrum, the proportion of an image showing "red" or "orange" was obtained, and used to set limits on protein packing density within the nanoparticle.

Comparative analyses Data for large natural nanoparticles were obtained from the published literature and used to derive the apparent average packing density for these particles. The nuclear pore was selected for this purpose because it consists of numerous sub-assemblies and thus resembles the nanoparticles reported here, which were prepared as assemblies of single albumin molecules.

Albumin immunohistochemistry

The presence of albumin-specific epitopes in the nanoparticles was checked by immunohistochemistry. In one series of immunostainings, nanoparticles were dried down onto formvar-coated nickel grids, and in a second series ultrathin sections of nanoparticles embedded in Epon were placed on nickel grids. For staining, grids were dipped 300× in distilled water, placed on 50 µl drops of PBS for 10 min, transferred to drops of PBS containing 1% gelatine B (blocking buffer) for 30 min at 37°C, then onto drops of blocking buffer containing 1:100 monoclonal mouse antibody to HSA (Sigma, A-6684) or 1:100 polyclonal rabbit anti-HSA (Dako, A0001) and incubated with this at 4°C overnight. Following thorough washing by 300 dips in distilled water (3 changes), the grids were incubated on drops of blocking buffer containing 1:30 goat anti-mouse immunoglobulins conjugated with 10 nm gold particles (Sigma, G7777) or gold-conjugated goat anti-rabbit immunoglobulins (Sigma, G7402), for 1 h at room temperature. Following thorough washing as before, grids were dried under a lamp. They were viewed in a Philips CM120 transmission electron microscope, without contrasting with lead and uranium salts.

Stability testing of the nanoparticles

Chelate stability of radiolabelled nanoparticles

The chelate stability of radiolabelled nanoparticles was tested by incubation in three different solutions: PBS, 4 mM DTPA solution pH adjusted to 7, and fresh human plasma over a period of 24 h at 37°C and determining the time dependent release of "free" ^{111}In by ITLC followed by electronic autoradiography. Additionally, the suspensions were kept at −20°C for a period of 10 half-lives of the radionuclide to demonstrate that the nanoparticles remained intact during chelate stability testing. After decay, the suspensions were fixed by mixing them 1:1 with 1% osmium tetroxide and incubated overnight. After

centrifugation, the pellet was mixed with 1% gelatin at 60 C, allowed to cool, the block thus produced was xed overnight in 2.5% glutaraldehyde, dehydrated in an ascending series of propyl alcohols, passed through acetone twice as intermedium and embedded in Epon. Ultrathin sections were viewed in a Philips CM120 electron microscope without contrasting in uranium and lead salts.

Structural integrity of the nanoparticles

Nanoparticles were tested in non-stabilised states, for stability against destructive in uences, including ultrasonication as a model for turbulence, exposure to detergents, heat, and various combinations of these agents. To test the effects of ultrasonication, nanoparticle samples, at concentrations 2–8 mg/ml in puri ed Millipore water, were exposed to ultrasound (35 kHz) in a waterbath for 10–20 min. To test the effects of detergent action, nanoparticle samples, 8 mg in 1.5 ml, were incubated at room temperature for 2 h in 1.5 ml SDS buffer containing 0.3–0.7% SDS, a 3× higher concentration than reported by other authors (Gururaj Rao and Narasinga Rao 1983). To test the effects of heat, nanoparticle samples, 2.5–16 mg in 1 ml water, were held at 60C for 1–2 h. To test the effects of exposure to blood plasma, nanoparticle samples, 0.5 mg in 200 µl or 2 mg in 1 ml, were suspended in plasma from fresh whole human blood, shaken in a waterbath at 37C for 1–4 h, and exposed to ultrasound for 5 of every 15 min, or for 2 of every 10 min. Following exposure to these potentially disruptive agents, the nanoparticle samples were prepared for TEM. Three sets of samples were examined. The rst set was mixed 1:1 with 1% uranyl acetate and dried onto EM grids for negative staining. The second set was centrifuged at 8,000×*g* for 10 min in order to ascertain whether a pellet could be obtained: a control pellet was prepared by centrifugation of a non-treated suspension containing a known weight of nanoparticles. In the test samples, the absence of a pellet after centrifugation indicated the absence of nanoparticle-sized material, implying total disruption of the nanoparticles. The presence of a pellet indicated the presence of particles or aggregated material, and the pellet was investigated by TEM. The supernate was discarded and the pellet xed in 5% glutaraldehyde in water, overnight at 4. The third set was xed by addition of an equal volume of 5% glutaraldehyde in water, incubation at 4C overnight, and then pelleted by centrifugation. All pelleted samples from sets 2 and 3 were rinsed free of glutaraldehyde, post xed in 1% osmium tetroxide overnight at 4C, dehydrated in ascending alcohols, passed through acetone as intermedium, and embedded in Epon. Ultrathin sections were cut at 90 nm thickness and then viewed in a Philips CM120 electron microscope without prior contrasting with heavy metal salts. Digital images were obtained at primary magni cations up to 120,000×.

Cytotoxicity testing of the nanoparticles

The toxicological properties of the nanoparticles were analysed in a hierarchical screening system aimed largely at determining their potential cellular toxicities. The assays which were used are suggested in the “Biological Evaluation of Medical Devices-part 5: Tests for in vitro cytotoxicity guidelines (ISO 10993-5:1999)” and “Biological Evaluation of Medical Devices-part 4: selection of tests for interaction with blood (ISO 10993-4:2002)”. An endothelial cell line, EAhy926, was used; derived from human umbilical vein endothelial cells, this cell line retains endothelial features to a high degree (Edgell et al. 1983; Unger et al. 2002) and is, therefore, relevant for testing nanoparticles for parenteral application.

Cell culture conditions

Medium used for the EAhy926 cells consisted of 90% Dulbecco’s modi ed Eagle’s medium, 10% FBS, 2 mM L-glutamate, 1% penicillin-streptomycin liquid. Cells were pre-cultured at 37C, 5% CO2, 95% relative humidity for 24 h prior to the exposure with the nanoparticles. Medium was removed, and new medium with particles (0–2 mg/ml) was added. All cytotoxicity assays were performed according to standard protocols and two exposure times (4 and 24 h) were evaluated.

LDH release assay

Experiments were performed in triplicate. The standard assay set-up included: blank (B, culture medium alone), growth control (GC, culture medium with the cells), lysis control (lysis, untreated cells in medium where 100% lysis was performed at the end of the exposure time), particulate positive control (PC, cells treated with 26 nm carboxyl White Polystyrene Latex, Invitrogen) and negative control (NC, cells treated with 160 nm Surfactant-Free Carboxyl White Polystyrene Latex, Invitrogen). To detect a potential interference of the particles with the assay the interference control (IC, particles without cells) was included. The CytoTox-ONE assay (Promega) was performed as indicated by the producer. Fluorescence was read with excitation of 560 nm and emission 590 nm with a uorometer (FLUOstar Optima, BMG Labortechnik). The average value of the blank was subtracted from every uorescence value. The percent toxicity was calculated according to the formula:

$$\text{Percent cytotoxicity} = 100 \times \frac{(\text{Experimental} - \text{CultureMediumBackground})}{(\text{Maximum LDH Release} - \text{Culture Medium Background})}$$

MTS test for cellular viability

The MTS assay (formazan bioreduction assay) was used to evaluate the viability of cells through the reduction of a tetrazolium salt to a coloured formazan salt by intracellular dehydrogenases. In the case of cell loss, decreased proliferation or unfavourable metabolic situations the activity of these enzymes and consequently the photometric signal is decreased. Cell seeding and exposure to the nanoparticles was the same as for the LDH-release, all controls with the exception of the lysis control were included. The CellTiter 96 Aqueous Assay (Promega) was performed as indicated by the producer and the absorbance at 490 nm read after 2 h at 37 C with a photometer (Spectramax Plus 384, Molecular Devices). The blank was subtracted from all other absorbance values.

Quantitation of ATP to measure cellular viability

Another method used to measure cellular viability was ATP-quantitation, giving information about the metabolic activity of the cells. This method uses the oxidation of luciferin to oxyluciferin by re y luciferase for detection. After treatment, the cells were lysed to release all intracellular ATP. Fire y luciferase activates luciferin by ATP and produces oxyluciferin and a burst of light. When ATP is the limiting component, the intensity of light is proportional to the concentration of ATP. As in formazan bioreduction, decreased cell number and an adverse metabolic situation can decrease the signal. Cell seeding and exposure to the nanoparticles was the same as for the LDH-release but no lysis control was included in the set-up. The CellTiter-Glo assay (Promega) was performed as indicated by the producer. Luminescence was detected by a LUMIstar (BMG Labortechnik). The blank was subtracted from all values.

Haemocompatibility testing of the nanoparticles

The assays which were used are suggested in the "Biological Evaluation of Medical Devices-part 4: selection of tests for interaction with blood (ISO 10993-4:2002)" and were approved by the local ethics committee.

Haemolysis

Erythrocyte suspensions were obtained by centrifugation of erythrocyte concentrates (Department of Blood Group Serology and Transfusion Medicine, LKH Graz) for 10 min at 1,200× *g* at RT. After removal of the supernatant, the pellet was suspended in PBS and centrifuged under the same conditions. This procedure was repeated twice until the supernatant was transparent. An erythrocyte suspension of 2% was prepared and incubated with the particles or PBS for 2 h at 37 C and thereafter centrifuged at 1,500 *g* for 5 min at RT. The degree of haemolysis was determined by the absorbance of haemoglobin at 540 nm in the supernatant. Absorbance at 100% haemolysis was determined by adding 10 µl of Triton X-100 (1%, *V*/*V*) to 1 ml of the erythrocyte suspension.

Quantification of prothrombin fragments F1 + 2 and of D-dimer

Fresh frozen plasma from healthy volunteers was incubated with particle suspensions or with PBS for 1 h at RT. As negative control, particles were omitted from the incubation. As positive control kaolinite (5 mg/ml) was used. For the quanti cations assay, Pro Human Prothrombin ELISA Kit (Hölzel Diagnostica) and TECHNOZYM Ddimer ELISA (Technoclone GmbH) were used. For prothrombin quanti cation, internal standards were prepared and incubation of the samples in the well, with competing biotinylated prothrombin, with streptavidin-peroxidase conjugate, with 3,3′,5,5′-tetramethylbenzidine as peroxidase substrate and with hypochloric acid as stop reagent were performed as indicated by the producer. For detection of the brinolysis product D-dimer, the incubation of the samples and standards in the well was followed by incubation with horse radish peroxidase-labelled antibody, with 3,3′,5,5′-tetramethylbenzidine as peroxidase substrate and with sulfuric acid as stop solution. Absorbance was read at 450 nm (650 nm as reference wavelength) with a Spectramax Plus 384 (Molecular Devices) photometer.

Quantification of activated complement (anaphylaxin C3a)

Fresh frozen plasma from healthy volunteers was incubated with particle suspensions or with PBS for 1 h at RT. As positive control Cobra Venom factor (10 U/ml) was used. The Quidel C3a EIA Kit was used for quanti cation of C3a-desArg, the stable degradation product of anaphylaxin C3a. Internal standards were prepared and incubation of the samples in the plate, with the horse radish peroxidase-labelled antibody, with 3,3′,5,5′-tetramethylbenzidine as peroxidase substrate and with sulphuric acid as stop solution were performed as indicated by the producer. Absorbance was read at 450 nm (650 nm as reference wavelength) with a Spectramax Plus 384 (Molecular Devices) photometer.

Storage of the nanoparticles

For periods of a few days, nanoparticles in suspension were stored at 4C. For longer periods, the nanoparticles were

frozen in liquid nitrogen and lyophilised (at −52 C and 58×10^{-3} Megabars).

Results

Chemical composition of the nanoparticles

The nanoparticles, synthesised by emulsifying HSA–DTPA–Gd conjugate with PLA, contained 3–5% PLA by weight; since the nanoparticles therefore consisted of 95% HSA–DTPA–Gd conjugate molecules, chemical analyses of them gave similar results as for the conjugates. The nanoparticles were designed for use in MRI, so the major feature of interest in their chemical composition was the number of Gd ions attached to each HSA molecule. This was assayed by several types of analysis. First, the conjugate exhibited molecular weight (MW) 80–90 kDa in polyacrylamide gel electrophoresis (PAGE), appearing as a relatively broad band (Fig. 2a). This indicated that the albumin molecules within any single batch were conjugated with varying numbers of the DTPA moieties chelating the Gd ions. Second, chemical analyses by the Pierce method and by UV_{280nm} absorption (to assay HSA) and by AAS (to assay Gd), determined the Gd:HSA ratio directly for each batch of conjugate and each batch of nanoparticles. This analysis revealed interbatch variability, in addition to the intrabatch variability seen in PAGE; in 10 batches of conjugate, the mean Gd:HSA ratio was 22 (standard deviation: 4) (Fig. 2b). The molecular weight of the conjugates was therefore close to 78.5 kDa ($MW_{Gd} = 157.25$ Da, $MW_{DTPA} = 393$ Da, $MW_{DTPA-Gd} = 550.25$ Da, $MW_{HSA} = 66.4$ kDa; $[22 \times 550.25] + 66{,}400 = 78.51$ kDa). This was consistent with the 80–90 kDa value obtained from PAGE (Fig. 2a).

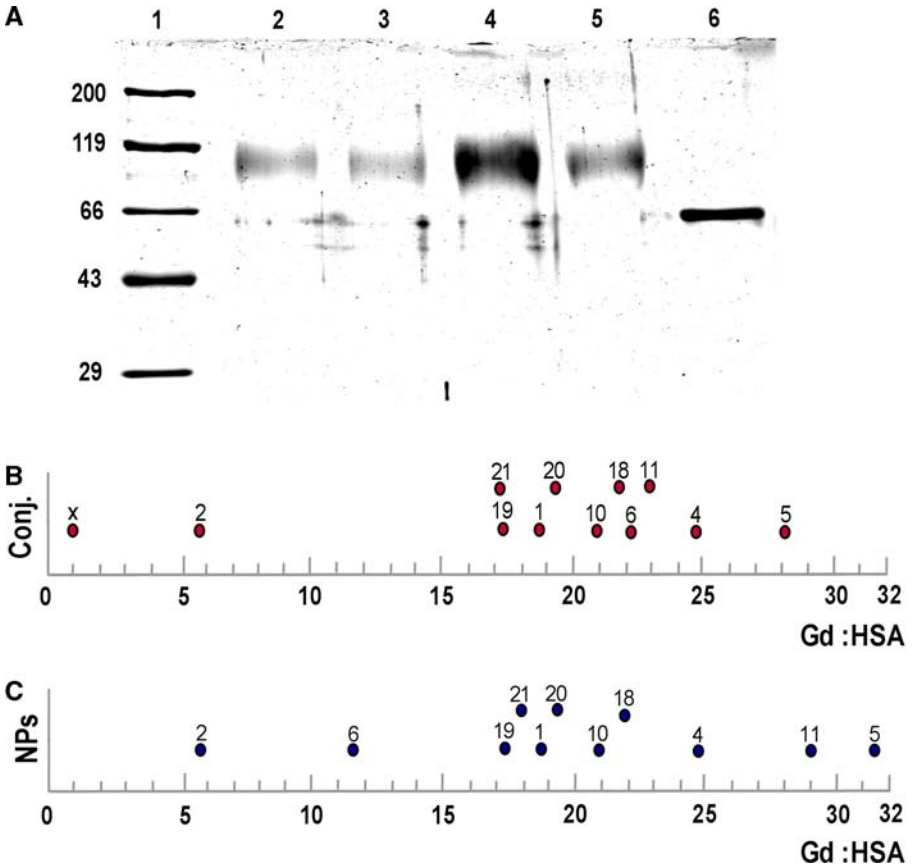

Fig. 2 a SDS gel electrophoresis of human serum albumin–(Gd–DTPA), human serum albumin and molecular weight standards. *Lanes 1* molecular weight standards, *lanes 2* and *3* HSA–DTPA–Gd (batch A) 2 and 1 μg, respectively, *lanes 4* and *5*, HSA–DTPA–Gd (batch L) 5 and 2 μg, respectively, *lane 6*, human serum albumin 2 μg. The vertical scale is not linear, being increasingly compressed at higher molecular weights. The broad bands in lanes 2–5 lie in the range 80–90 kDa. b This dot diagram shows the Gd:HSA ratios for 12 batches of HSA–DTPA–Gd conjugates, one dot for each batch. The batch identi cations are stated as numbers between 1 and 21; X was an early batch in development of these conjugates, and together with batch 2 was excluded from further analysis because synthesis had failed. Two further batches (not shown here) with extremely high Gd:HSA values (60–100) were also excluded because puri cation had failed. The mean value of the batches clustered between 15 and 30 was 22, and this was the value used in relaxivity calculations. c This dot diagram shows the Gd:HSA ratios for 11 batches of nanoparticles. The batch identi cations are stated as numbers between 1 and 21

The nanoparticles prepared from these HSA–DTPA–Gd conjugates had a slightly lower Gd:HSA ratio = 19 (Fig. 2c), so the HSA–DTPA–Gd molecules within the nanoparticles had lower molecular weights, MW = 76.9 kDa. The chemical composition of the conjugates and nanoparticles were re ected in their relaxivity properties in MRI (Table 1, and see below). Within the nanoparticles, the HSA retained its molecular form, as demonstrated by the positive immunohistochemical reactions obtained by use of both monoclonal and polyclonal anti-HSA antibodies to test both the conjugate (not shown) and also the nanoparticles (Fig. 3). Positive immune reactions obtained after heating the nanoparticles at 60°C for 2 h indicated that the molecular conformations within the nanoparticles were heat-resistant, and therefore stable.

Physical properties of the nanoparticles

Size of the nanoparticles measured by TEM

Visualising the HSA molecules in negative contrast by TEM allowed accurate measurements of their size, which was close to 10 nm (Fig. 4a). The same procedure applied to the nanoparticles, with magni cations in the range ×100,000, showed them as white rounded ovoids, with rough edges, against a dark background; they appeared as single particles and showed no signs of aggregation (Fig. 4b). Low magni cation images, in the range ×40,000, allowed approximately three thousand nanoparticles to be seen in a single eld of view, demonstrating the lack of aggregation and providing an immediate assessment of size variability; one of the earliest batches (batch #1), shown in Fig. 4c, consisted of unusually small nanoparticles, with mean diameter 14 nm, and with a (high) polydispersity index = 1.43. Stating the size data for this batch in a different way, as mean and standard deviation, these nanoparticles had an average diameter ± 14 nm. Examination of numerous other batches showed that the procedures used in preparing and storing the nanoparticles, including glutaraldehyde stabilisation, osmium tetroxide xation, and lyophilisation, did not alter the nanoparticle sizes.

Size of the nanoparticles measured by PCS

PCS measurements provided rapid estimates of nanoparticle size, showing them to be approximately 35 nm diameter (Fig. 5a, b). PCS revealed rapidly any deviations from the usual 35 nm diameter, for example see the relatively pure batch of rather small nanoparticles shown in Fig. 5c, or the total failure to form any nanoparticles at all in another batch, Fig. 5d. PCS detected aggregates with high sensitivity (Fig. 5a, b). In most batches, aggregation was present only in vanishingly small degree, but in some batches, it was extensive: for example, in those shown in Fig. 5a, b aggregates could account for as much as two thirds of the nal product mass. As evident from the four problem batches shown in Fig. 5, PCS provided a rapid eal-time tool allowing rapid acquisition of size and aggregation data, and this was useful in guiding iterative development of the synthesis protocol.

The size and variability data from TEM and PCS are summarised in Fig. 6. All measurements showed the nanoparticles to be less than 100 nm diameter. The TEM size data clustered between 15 and 40 nm. The PCS size data included a cluster between 10 and 35 nm but with a few data points spread between 60 and 100 nm. In such cases, where PCS data diverged widely from TEM data, we rechecked the TEM analysis, and in each case, the PCS data was in error. Both the TEM and PCS size variation data showed a wide spread and indicated that within certain batches particles could vary considerably in size (PDI >2.0). The PDI value >2.0 indicated wide variation within a batch, for example: PDI = 1.5 showed a narrower size distribution than PDI = 2.0, but for particles of 25 nm diameter it indicated an average size of 25 nm diameter with standard deviation SD = 17.7 nm, so the particles were 25 ± 17.7 nm in diameter. TEM data indicated higher variability in nanoparticle sizes than did PCS data, probably due to the absolute numbers of particles sampled (the difference in sample sizes is 11 orders of magnitude). The clustered data in TEM and PCS are suf ciently close to one another to indicate that the standardised synthesis procedure generally produced nanoparticles in the size range 15–35 nm diameter. Both TEM and PCS data indicated a signi cant variability between successive batches, even although these were produced using a standardised protocol.

Shape and internal texture of the nanoparticles

Nanoparticles embedded in Epon and viewed in TEM were spheroidal, with rough surfaces. Shortly after emulsi cation, they appeared as micelles (Fig. 7a). Osmium post xation increased the micelles' electron density slightly, without reducing their size and without smoothing their surfaces. The electron-dense shell, presumed to be mainly the protein component, occupied ~95% of the micelle volume, and the electron-translucent core, presumed to be rich in PLA, occupied < 5% of the volume. Subsequent to lyophilisation the nanoparticles appeared amorphous, their reticulate structure intercalated with uid- lled spaces, their average sizes unaltered by the lyophilisation (Fig. 7b). In some nanoparticle samples embedded in Epon there was observed a characteristic type of contamination, which consisted of numerous large (~200 nm diameter), electron-dense nanoparticles of characteristic appearance (Fig. 7c). These were extremely electron-dense and were nally identi ed as

Table 1 Relaxivity data for conjugates and for three typical sizes of nanoparticles, measured and calculated using the Gd:HSA values shown in Fig. 2b and Fig. 2c

	Mass (Daltons) (calculated)[a]	No. of conjugate molecules per nanoparticle (calculated)	No. of Gd ions per conjugate molecule (measured)	No. of Gd ions per particle (calculated)	Relaxivity		Relaxivity		Relaxivity per Gd ion	
					r_1 (ml/mg s)[b] (measured)	r_2 (ml/mg s)[b] (measured)	r_1 (1/Ms) (calculated)	r_2 (1/Ms) (calculated)	r_1 (1/Ms) (calculated)	r_2 (1/Ms) (calculated)
Gd-DTPA chelate	550.25	/	/	1.00			4,623	5,786	4,623	5,786
HSA–DTPA–Gd conjugate	78,505.5	/	22[c]	22	1.8	2.5	141,310	196,264	6,423	8,921
Nanoparticle 20 nm diameter	1.42×10^6	18.5	19[d]	352	1.6	2.3	2.27 x 10^6	3.27 x 10^6	6,449	9,290
	0.82×10^6	*10.7* (each of mass 76,854.75 Daltons)		*203*			*1.31×10^6*	*1.89×10^6*	*6,453*	*9,310*
Nanoparticle 25 nm diameter	2.41×10^6	31.4	19[d]	597	1.6	2.3	3.86 x 10^6	5.55 x 10^6	6,466	9,296
	1.39×10^6	*18.1* (each of mass 76,854.75 Daltons)		*344*			*2.22×10^6*	*3.20×10^6*	*6,453*	*9,302*
Nanoparticle 30 nm diameter	4.77×10^6	62.1	19[d]	1,180	1.6	2.3	7.63 x 10^6	10.97 x 10^6	6,466	9,297
	2.74×10^6	*35.7* (each of mass 76,854.75 Daltons)		*678*			*4.38×10^6*	*6.30×10^6*	*6,460*	*9,292*

In the lower three rows, values shown in italics are calculated for packing density $\delta = 0.23$, the values above them for $\delta = 0.40$

[a] The dalton-gram conversion was carried out using the factor: 1 Da = 1.66054^{-24} g (which is one-twelfth of the mass of the carbon 12 isotope). The density of the nanoparticles was measured as close to 1.4 g.cm^{-3} (unpublished data)

[b] Mean value for conjugates; mid-range value for nanoparticles

[c] 22 Gd:HSA in the conjugates is taken as the mean value derived from the data in Fig. 2b

[d] 19 Gd:HSA in the nanoparticles is taken as the mid-range value of the cluster near 20 in Fig. 2c

$MW_{Gd\text{-}DTPA}$ is 550.25, so the MW of the HSA–DTPA–Gd molecule bearing 19 Gd ions is [(550.25 × 19) + 66,400] = 76,854.75 Da

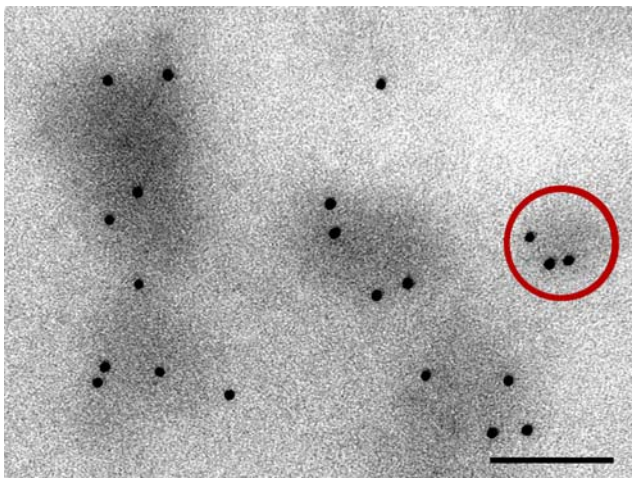

Fig. 3 Clusters of nanoparticles on a Formvar grid, labelled by immunohistochemistry for HSA, with gold-conjugated secondary antibody, gold particles 10 nm diameter. Most of the electron-dense structures shown here are clumps of several nanoparticles, the particle ringed with *red* is approximately 75 nm diameter: rather large to be a single nanoparticle. Negative controls and controls in which the primary antibody was blocked by antigen pre-incubation, both lacked labelling by gold particles (data not shown)

nanoparticles composed of metallic osmium; brief investigation showed that they could be prepared in pure form by mixing osmium tetroxide with 70 or 100% alcohol, and embedding the precipitate in Epon. Samples of albumin-based nanoparticles embedded in Epon did not contain these osmium nanoparticles if the osmium post xation step was followed with thorough rinsing (Fig7d). For comparison, negative-contrasted particles from a stability experiment are shown in Fig.7e.

Packing densities of the nanoparticles

From data such as that shown in Fig7a, and depending on the thresholding values employed during image processing, the packing density (δ) of the nanoparticles was measured to be $\delta = 0.35$–0.45. In contrast, from the published data for the nuclear pore complex, which has a diameter 98 nm, a channel width ~ 35 nm and a depth of ~ 40 nm (Alber et al. 2007a, b), it was necessary to assume an average packing density of $\delta = \sim 0.23$ in order to reach agreement with the value of ~ 50 MDa for the mass of the nuclear pore complex as stated by Alber's group.

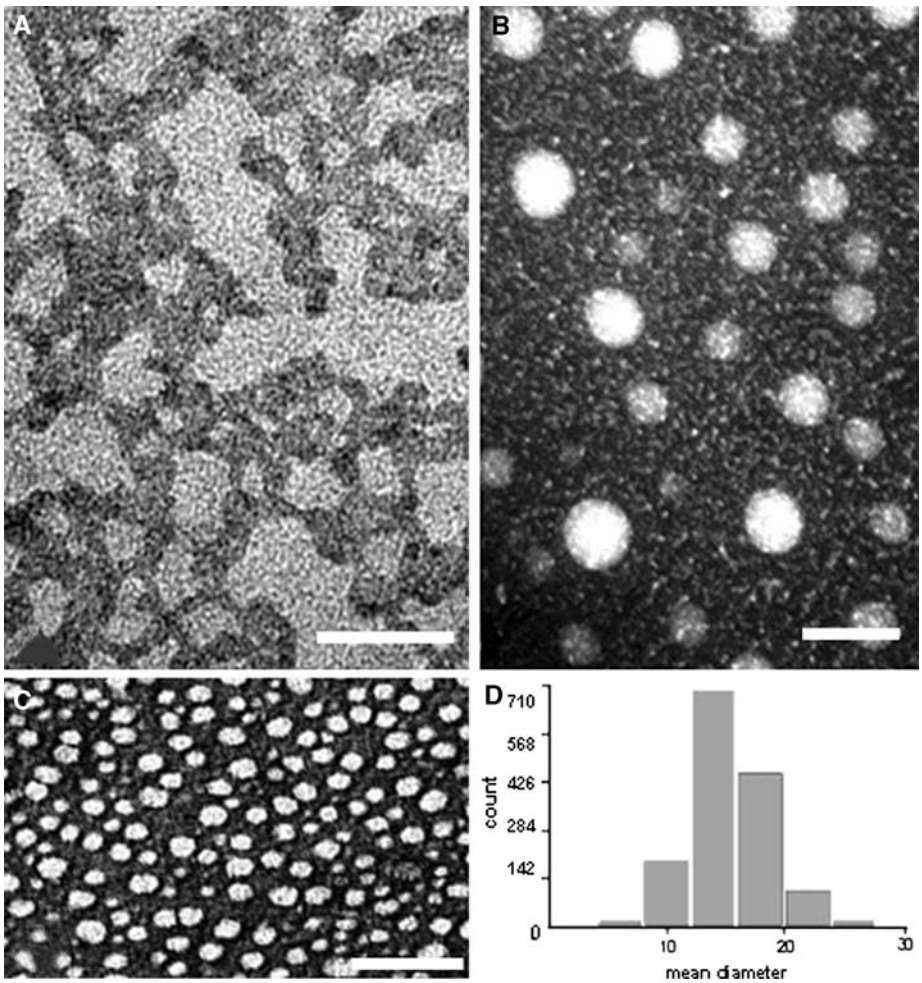

Fig. 4 a Particles of HSA in negative contrast TEM. Calibration *bar* 20 nm; original mag. b Negative contrast staining with 3% uranyl acetate. Calibration *bar*: 100 nm; original magni cation ×88,000. c Negative contrast imaging of nanoparticles (batch #1) by TEM. The 179 nanoparticles in this eld were enlarged from an image containing almost 3,000 nanoparticles, with primary magni cation ×40,000. The eld shown here is typical of the entire image, that is: no aggregates were present. Calibration *bar*: 100 nm. d Histogram of nanoparticle size frequencies for the total population of the nanoparticles shown inc. The absolute numbers of nanoparticles with a given diameter (nm) are shown. The mean value for this population is 14.0 nm, the standard deviation is 9.2 nm, the dispersity (PDI) is 1.43

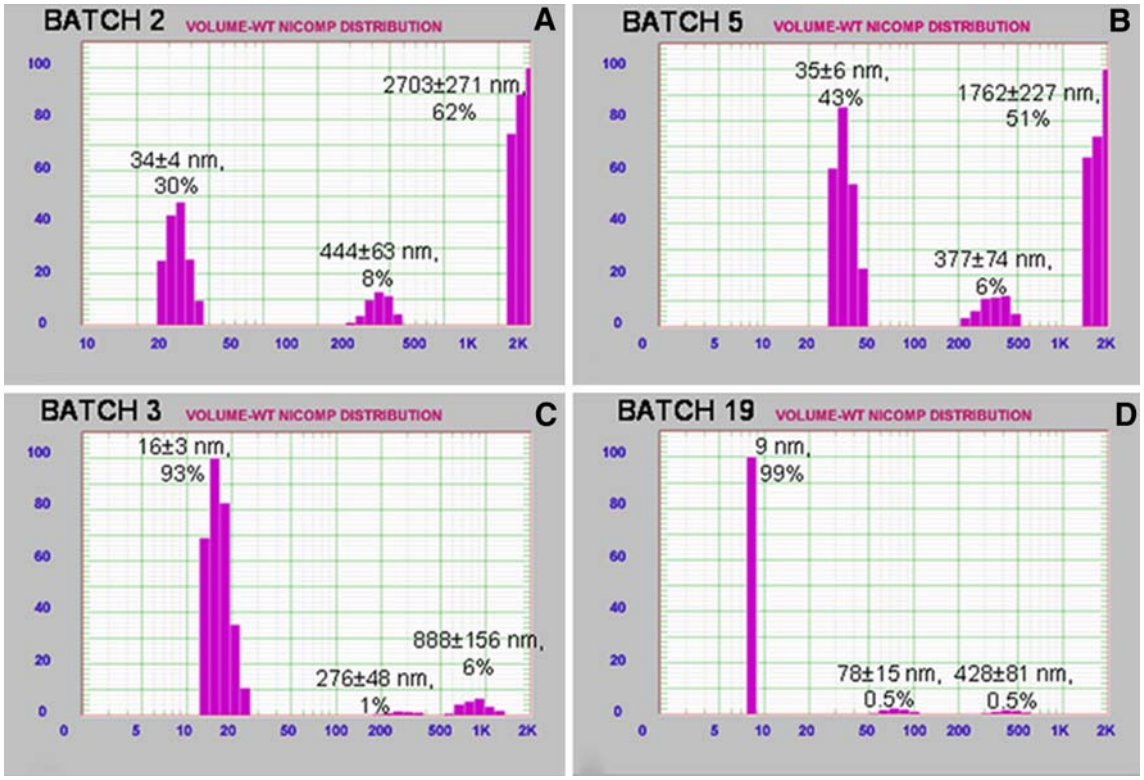

Fig. 5 Volume-weighted PCS read-outs of nanoparticle size distributions; three early batches, #2, #3 and #5, are shown, together with the late batch #19. **a**, **b** Batches #2 and #5 contain nanoparticles of typical sizes, close to 35 nm, and these data show that lyophilisation of the nanoparticles, followed by 18 months storage at 4°C (batch #5) does not alter significantly the degree of clumping and aggregation from that seen in freshly prepared samples (batch #2). To aid understanding of the read-outs, each size peak is labelled with its mean and standard deviation, and with the percentage of the total particle population that this peak represents. Note that the *x*-axis has a logarithmic scale in each read-out. **c** Batch 3 shows how PCS data rapidly reveal major features of a batch: in this case, that the batch contains few aggregates but that the nanoparticles are much smaller than usual. **d** Batch 19 shows total failure to form nanoparticles; the peak at 9 nm diameter represents HSA, the major primary ingredient, with its molecular size of 3 × 8 nm

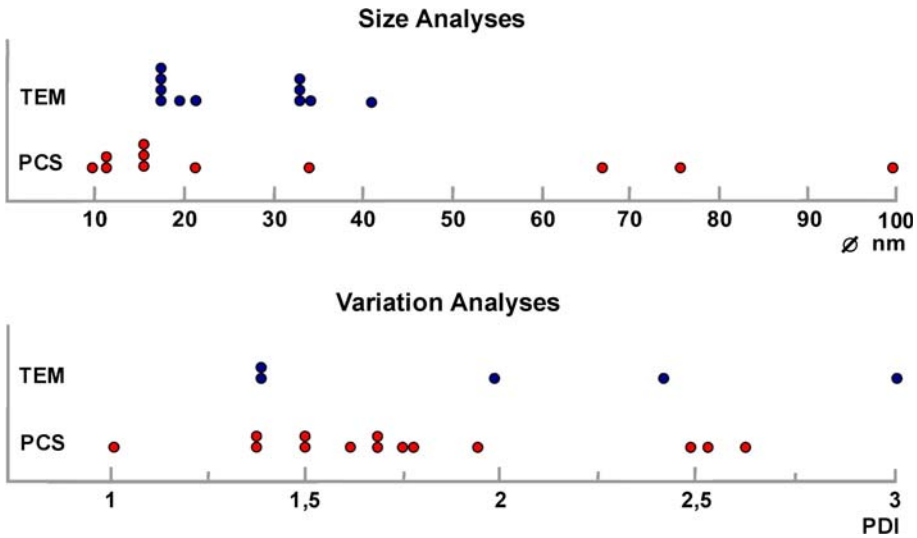

Fig. 6 Dot diagrams presenting size data for several nanoparticle batches (*upper panel*), and size variation data (*lower panel*) in the same batches. In each panel, one dot shows the data for a single batch of nanoparticles; each panel compares TEM data with PCS data. The size data are given as diameter in nanometers, the size variability data is given as PDI (scalar units)

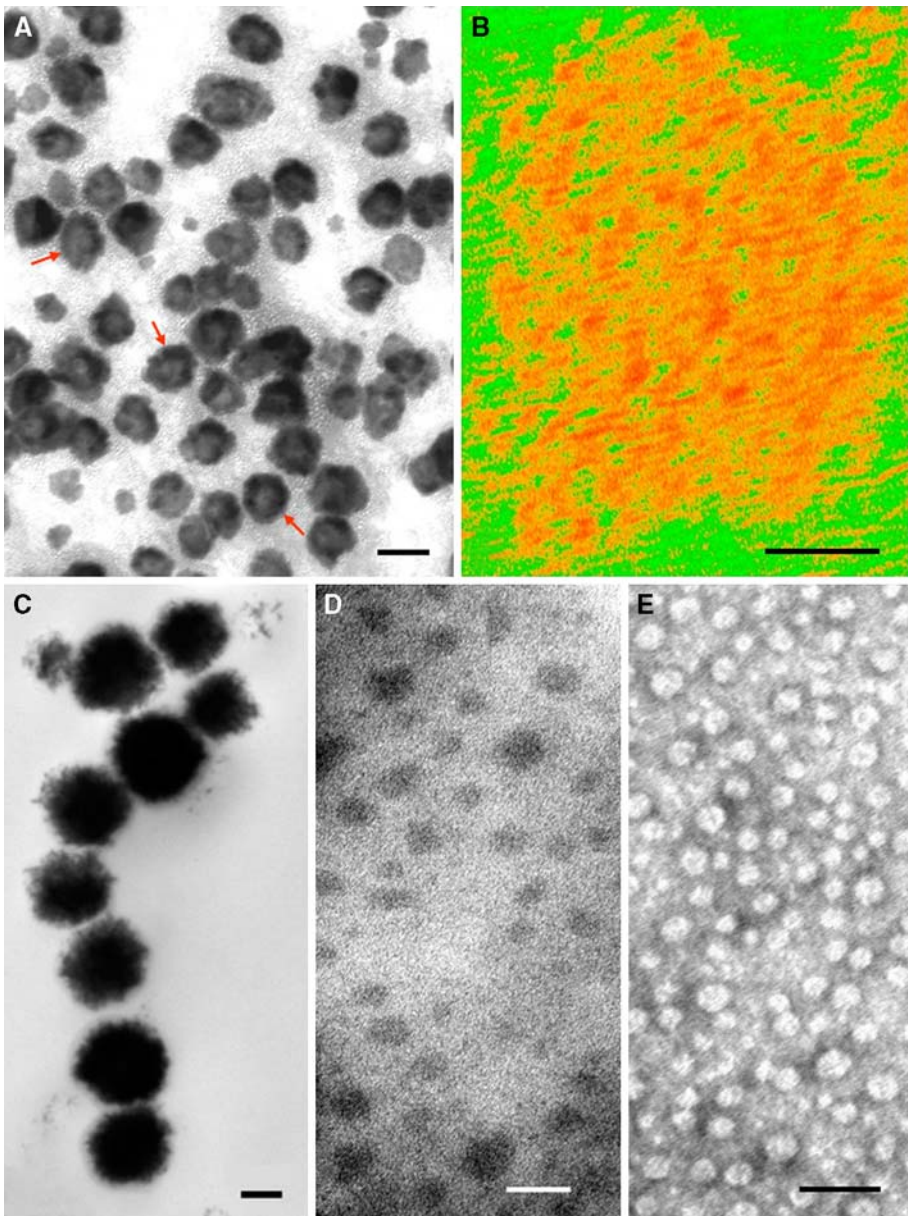

Fig. 7 a Nanoparticle from batch #1, in micellar form prior to lyophilisation. Due to spatial sectioning artefacts, the annulus characteristic of micelles is not clearly visible in each particle. *Red arrows* point to three micelles with complete annuli. Glutaraldehyde xation followed by osmium tetroxide post xation for transmission electron microscopy. Calibration *bar* 100 nm. b Nanoparticle from batch #1, after lyophilisation. Glutaraldehyde xation followed by transmission electron microscopy. The image is colour coded for grey shade differences. Calibration *bar* 10 nm. c A gure showing the osmium nanoparticles: this is a spurious result. Calibration *bar* 100 nm. d A gure showing the nanoparticles in Epon. This sample was washed thoroughly after xation in osmium tetroxide. It shows how nanoparticles would be expected to appear in tissue samples derived from animal studies. Calibration *bar* 100 nm. e A gure showing the nanoparticles in negative contrast after disruptive treatment: plasma, heat and ultrasound. Calibration *bar* 100 nm

Number of albumin molecules and gadolinium ions in an average nanoparticle

A nanoparticle of 15 nm diameter has a volume of 1,767 nm^3, large enough to contain only 8 albumin molecules (of volume each ~ 90 nm^3) at a packing density $\delta = \sim 0.40$, or 4.6 albumin molecules at a packing density $\delta = \sim 0.23$. However, a nanoparticle of diameter 30 nm has a volume of 14,140 nm^3, large enough to contain 64 conjugate molecules at a packing density $\delta = \sim 0.40$, or 37 albumin molecules at a packing density $\delta = \sim 0.23$. Since the albumin–DTPA conjugate molecules each bore ~ 20 Gd ions, then a nanoparticle of diameter 30 nm contained 750–1,300 Gd ions (the exact number depending on the packing density). Table 1 calculates detailed examples based on measurements of nanoparticles prepared by the protocols described here.

Surface charge measured as zeta potential

The HSA–DTPA–Gd conjugates carried a small positive charge, between +1 and +3 mV. The nanoparticles, in contrast, were negatively charged, varying between −17 to −41 mV. Lyophilisation reduced the charge, and resuspended nanoparticles after lyophilisation had charge close to −5 mV.

MR relaxivity of the conjugates and nanoparticles

Relaxivities were measured for both the HSA–DTPA–Gd conjugates and the nanoparticles. The primary data consisted

of plots relating MR proton relaxation rates R_1 and R_2 to concentrations of the test substance; from these plots the relaxivities were calculated as the slopes of the plotted lines. It was necessary to standardise the conditions for measurements, because a range of factors influenced the results. Temperature was one of these factors: for both the conjugates (not shown) and the nanoparticles (Fig. 8a, b), relaxation values were higher at higher temperatures. The chemical constitution of the medium could also affect the values measured: for example, although the same relaxation rates were measured for conjugates (Fig. 8c) and for nanoparticles (Fig. 8d) suspended in phosphate-buffered saline or in water, higher rates were measured for the same particles suspended in blood plasma (Fig. 8d). Relaxivity values r_1 and r_2 of the test substance were first calculated as rates expressed in terms of the substance concentration (ml/mg second). Figure 9a shows the spreads of relaxivity values obtained for the conjugates in terms of absolute weights (ml/mg s). In a further step of calculation, the relaxivities were expressed as rates in terms of molar masses (1/Ms), calculated by factoring in the molecular masses expressed in kiloDaltons (kDa) as calculated from PAGE, AAS and Pierce assay data (see above) (Fig. 9b). A final step of calculation derived the relaxivity of the test material in terms per Gd ion (see Table 1b). Similar plots and calculations were carried out for the nanoparticles (Figs. 9c, d). Since relaxivity expressed in terms of particle mass depended on the particle size, data concerning nanoparticle diameter was tabulated (Table 1) for three different nanoparticle sizes in the relevant range: 20, 25 and 30 nm diameter. The relaxivity values obtained for the nanoparticles lay in the range $r_1 = 2.27 - 7.63 \times 10^6$ 1/Ms and $r_2 = 2.27 - 10.97 \times 10^6$ 1/Ms. The precise relaxivity of a particular suspension of nanoparticles depended on the mixture of the different sizes of nanoparticles present in the suspension. A suspension of nanoparticles with average diameter 25 nm therefore exhibited average relaxivity $r_1 = 3.86 \times 10^6$ 1/Ms, but a few particles in the suspension would have relaxivities as low as $r_1 = 1.75 \times 10^6$ 1/Ms and a few

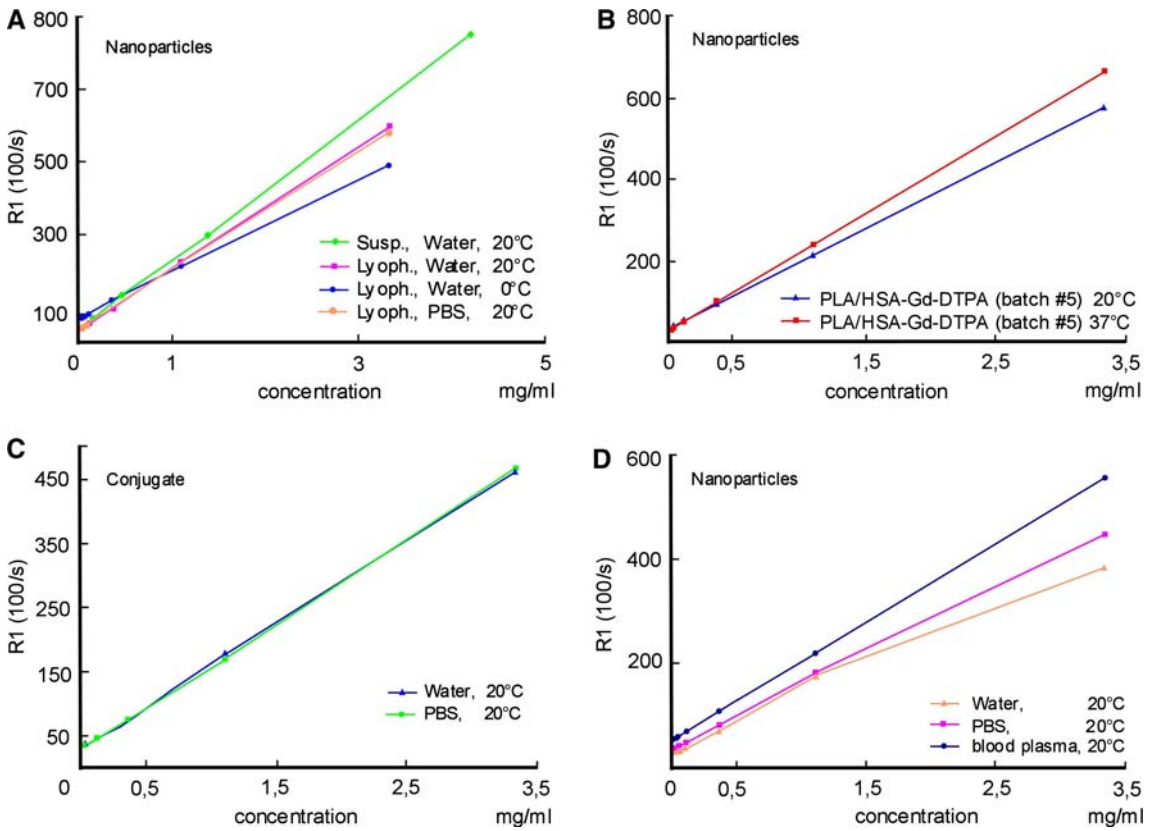

Fig. 8 a Measurements of nanoparticle relaxation rates, for a single batch of nanoparticles. The relaxation rate is read from the slope of the graphed lines. The measurement at room temperature shows a clearly higher R_1 relaxation rate as compared to measurement at 0 °C. b Relaxation rates plotted for the same batch of nanoparticles as shown in a. The significant enhancement of R_1 by raised temperature (37 °C compared with 20 °C) is clearly visible. c MR relaxation rates plotted for a single batch of HSA–DTPA–Gd conjugate. The relaxation rate (here R_1) is the same in water and in PBS. d MR relaxation rates R_1 plotted for a different batch of nanoparticles. As with the conjugate shown in c, suspending the nanoparticles in water or in PBS results in closely similar slopes in the plots, whereas nanoparticles suspended in blood plasma exhibit a significantly higher relaxation rate

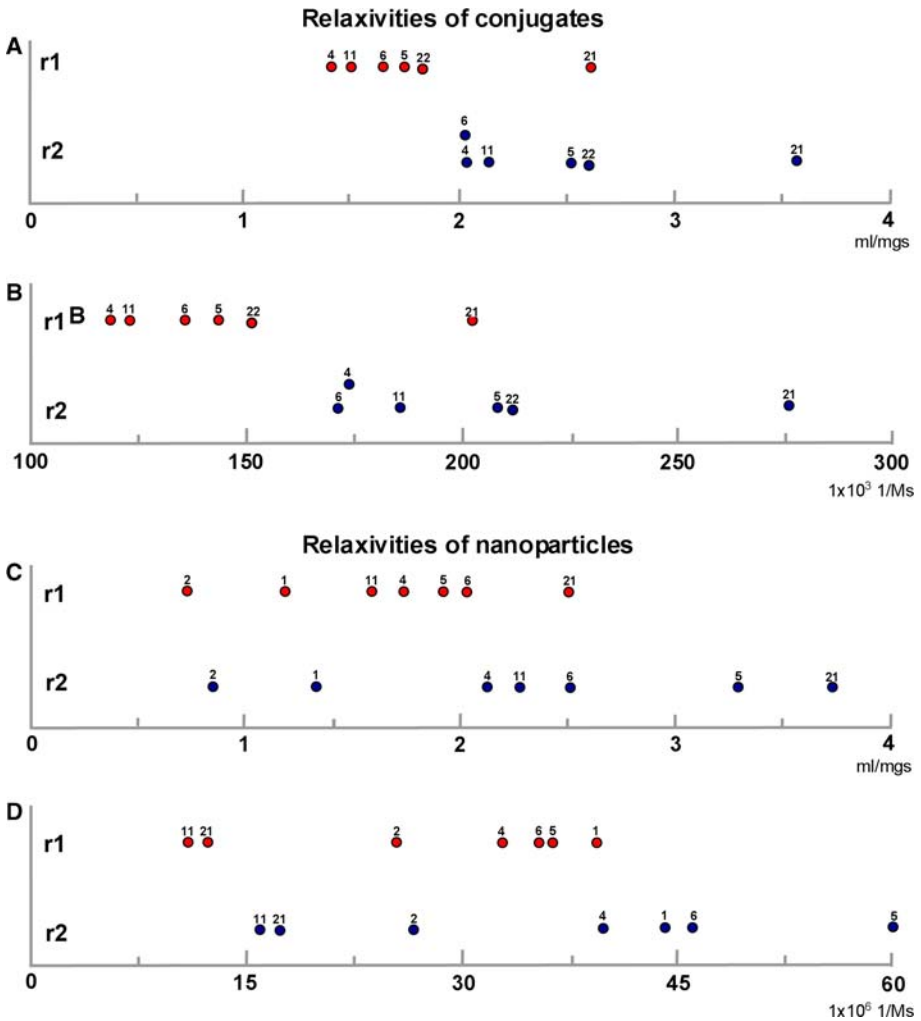

Fig. 9 a Dot diagram showing relaxivity data for conjugates, presented as mg/ml s. The mean value for r_1 is: 1.82 ml/mg s (SD = 0.40 ml/mg s); the mean value for r_2 is 2.57 ml/mg s (SD = 0.51 ml/mg s).b Dot diagram showing relaxivity data for conjugates presented as 1/Ms. The mean value for r_1 is: 144,684/Ms (SD= 28,534/Ms); the mean value for r_2 is 204,122/Ms (SD= 36,769/Ms). c Dot diagram showing relaxivity data for nanoparticles presented as mg/ml s. The mean value for r_1 is: 1.70 ml/mg s (SD = 0.54 ml/mg s); the mean value for r_2 is 2.35 ml/mg s (SD = 0.94 ml/mg s).d Dot diagram showing relaxivity data for the nanoparticles. Each dot shows the data for a single batch of nanoparticles. The relaxivities r_1 and r_2 are shown separately, in the appropriate units (1/Ms, where M= Mole weight and s= seconds). This calculates in the mass of the nanoparticles (4.77 MDa, see Table 1), and therefore the number of Gd ions attached to the nanoparticles. The mean value for r_1 is: 8.12×10^6/Ms (SD = 2.58×10^6/Ms); the mean value for r_2 is 11.21×10^6/Ms (SD = 4.48×10^6/Ms)

would have relaxivities as high as $r_1 = 6.67\ 10^6$ 1/Ms; similar considerations apply to the relaxivity value r_2. For a suspension of nanoparticles with diameter 25 nm and at 20 C, these relaxivity values implied that a concentration of 1–2 mg/ml of nanoparticles in the uid was required to enhance MR relaxation rate in a column of uid (such as a blood vessel) by a factor 3 (compare Fig. 8a, b, d). As noted above, the necessary concentration would be slightly lower in the presence of blood plasma, or at higher temperature.

Stability of the nanoparticles

Two types of stability were tested. The rst was the structural integrity of the nanoparticles, their stability as solid masses, assayed by particle resistance to break-up under stress in the form of turbulent conditions, during heating, or in corrosive uids such as blood—and in blood during heating and turbulence. The second was the stability of the metal chelation, measured as the rate of ^{111}In release from the DTPA chelator under exposure to different chemical milieus.

Structural integrity of the nanoparticles

Most types of destructive testing left the nanoparticles intact: heat at 60 C, ultrasonication, and incubation in human blood plasma. Combination of these potentially destructive agents also failed to disrupt the nanoparticles. The particles did not decompose under heating to 60 C, or when exposed to prolonged bouts of ultrasound, and retained their integrity for hours in heated fresh blood plasma, even when this plasma was exposed to ultrasound. Furthermore, at the end of testing, the nanoparticles remained as individual, single particles, and had not formed aggregates (Fig. 7e). The failure of these testing conditions to destroy the nanoparticles suggested they would remain intact in turbulent blood ow. Only one treatment was found to disrupt the nanoparticles: incubation in SDS detergent.

Table 2 Time dependent release of free ^{111}In from radiolabelled nanoparticles incubated in PBS, 4 mM DTPA solution and fresh human plasma

Incubation time	1 h	2 h	4 h	24 h
^{111}In-HSA-DTPA/PLA [%]				
PBS	98.4± 0.5	96.2± 3.7	95.9± 3.1	92.7± 6.8
DTPA	94.4± 5.3	91.8± 4.5	92.0± 3.7	86.1± 9.8
Plasma	96.7± 5.6	94.7± 5.9	96.5± 1.8	88.5± 9.6

Values are expressed as percentage of radioactivity related to "free" radionuclide determined using instant thin layer chromatography (mean± SD, $n = 6$)

Chelate stability of radiolabelled nanoparticles

Release of "free" radionuclide was observed from the ^{111}In-labelled nanoparticles incubated in different media, during an observation period of 24 h (Table 2). In PBS > 92% of ^{111}In remained in chelated form 24 h after incubation. In human blood plasma the corresponding value was >88%, and in 4 mM DTPA solution it was >86%. This represented loss of ^{111}In out of the chelate between 7–14% in 24 h, depending on the composition of the medium. Ultrastructural examination after decay showed that the nanoparticles resisted the radiolytic effects and retained their morphological integrity.

Nanoparticle cytotoxicity

One batch of nanoparticles was examined in detail. Two independent assays for cell viability were used: the first was the MTS test, which used formazan bioreduction to measure the activity of intracellular dehydrogenases, and the second was assessment of ATP-content as indication for the metabolic state of the cells. Both tests are used as indirect tests for cell number and cell proliferation. No negative effects of the Gd-loaded HSA nanoparticles on cell physiology and cellular integrity were observed. After 4 h and after 24 h, the particles did not cause a decrease in formazan bioreduction (Fig. 10a) or in ATP content: the cells remained viable. As nanoparticles may disrupt cellular integrity, in addition to the assessment of viable cells the lactate dehydrogenase (LDH) release assay was performed. Furthermore, the proportion of cells with membrane damage as assessed by LDH-release remained equally as low in cells incubated with nanoparticles as in untreated cells (Fig. 10b). Tested in erythrocyte suspensions, the particles caused less than 1% haemolysis. There was no indication of any alteration in coagulation or in activation of the complement system: the levels of complement C3a in the plasma were 133.2–427.3 ng/ml (within the normal range 100–250 ng/ml); levels of prothrombin and D-dimer were also in the normal range and close to those of plasma controls incubated without nanoparticles (Fig. 10c).

Synthesis yields

In two cycles of development, we developed standardised synthesis protocols for HSA nanoparticles, feeding back physicochemical characterisation data into the design process. In the first series of syntheses, yields were less than 50 mg per batch due to constraints associated with the purification apparatus, and were too small for extensive characterisation followed by pharmacokinetic studies. It was therefore not useful to optimise synthesis efficiency, instead it was necessary to modify the entire synthesis protocol to achieve at least a tenfold higher total yield. In the second series of syntheses, using dialysis for purification, yields were in gram amounts: in a typical synthesis, 5 g HSA yielded 5.3 g HSA–DTPA–Gd conjugate, which yielded 4.3 g nanoparticles. At the end of this iterative development, batch sizes were therefore large enough to provide sufficient materials for pharmacokinetic studies in animal and human models (manuscript in preparation).

Discussion

Any molecular imaging platform for use in MRI requires large signal amplification, and must therefore take the form of a nanoparticle (Debbage and Jaschke 2008). The present sensitivity levels of MRI mandate the presence of mg/ml concentrations of gadolinium in a liquid column to enhance contrast for imaging. For use in humans, batch sizes must therefore be measured in grams. This project aimed to develop standard protocols for synthesis of gram amounts of well-characterised nanoparticles for use in MRI. The attachment of Gd to HSA, then production of nanoparticles from the resulting conjugate, provided the platform needed for MRI. None of the nanoparticle components was new. HSA is familiar both in the clinic for use in critical care (Cochrane Report 1998; Colgan et al. 2000; Finfer et al. 2004; Wilkes and Navickis 2001), and recently in oncology (Gradishar et al. 2005), and also in the laboratory and in industry as a surfactant for a range of polymers. HSA–DTPA–Gd was carefully studied over several years by Brasch's group (Daldrup-Link and Brasch 2003) and is available commercially (for example, http://www.biopal.com). PLA is approved for clinical use in surgical implants. Both HSA alone and the HSA-PLA combination have been used previously to create microspheres (Boury et al. 1997; Kramer 1974; Montisci et al. 2001; Soriano et al. 1995; Tomlinson and Burger 1995). The novel aspect of the present study lies in its careful and extensive characterisation of the nanoparticles and in the search to

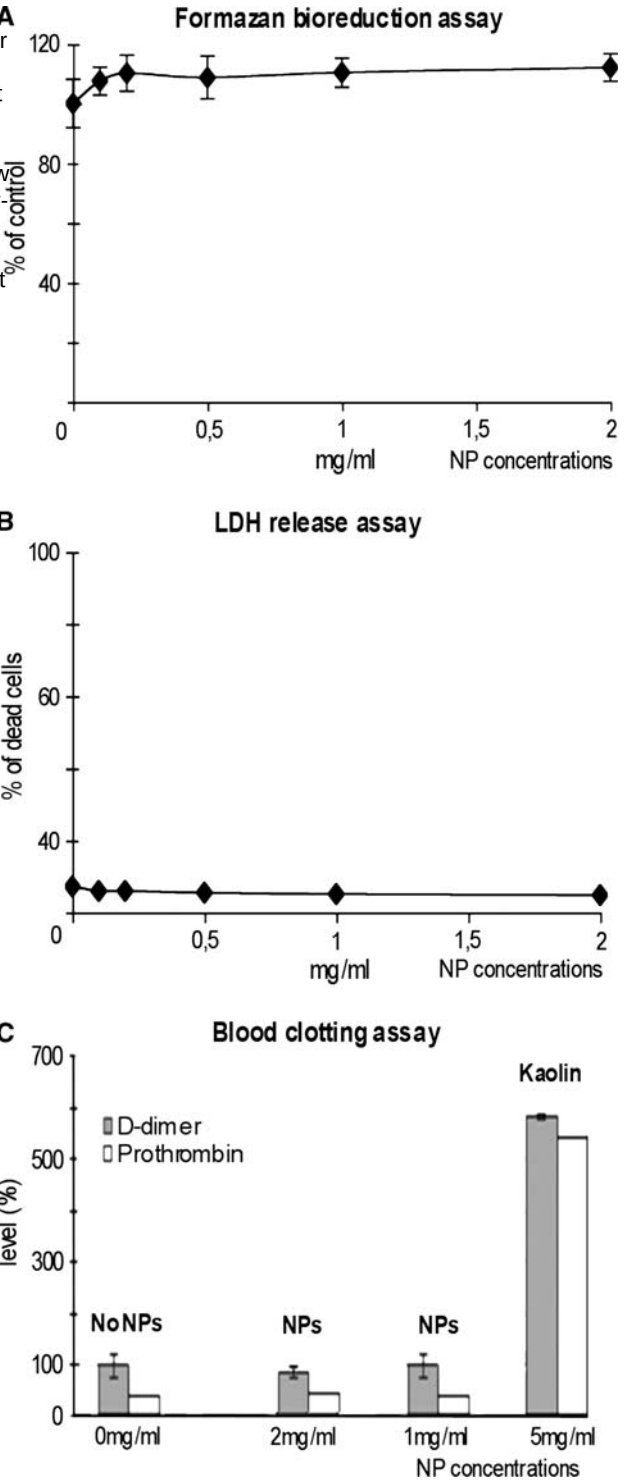

Fig. 10 Toxicological in vitro characterisation of Gd:HSA particles. Data are presented normalised to untreated cultures and blood or plasma samples as 100%. **a** MTS test for cell viability, a formazan bioreduction assay at different nanoparticle concentrations, and at incubation times of 4 and 24 h: the cells show no decrease in viability at any concentration of nanoparticles at 24 h, as shown by the LDH release assay at different nanoparticle concentrations: the cells show no evidence of membrane damage at any concentration of nanoparticles. **c** Blood clotting assays at different nanoparticle concentrations, at 1 h incubation, with kaolin as positive control and with nanoparticle-free suspensions as negative control. The nanoparticles did not increase prothrombin and d-dimer levels above the level of the negative control, and see comparison with the positive control

identify critical control points in the synthesis protocol, in order to allow ne-tuning of the method to produce exactly speci ed nanoparticles of a pre-de ned size. Several challenges were met and overcome during this development procedure. Since similar challenges await others who develop nanoparticles, so they will be considered here. The *first* was production of adequate amounts for physico-chemical analysis and for testing in animal models. To prepare the way for later industrial scaling up, the laboratory synthesis protocol should be scaled to produce batches at least one gram in size. This was achieved in this study by the nal protocol routinely generating 3–4 g of 30 nm diameter nanoparticles. A single batch of these nanoparticles was large enough to be used for extensive characterisation and testing, including testing in animal models. The major developmental step necessary to achieve large batch size was to replace FPLC as puri cation method, because this produced batches only 10–20 mg in size.

The *second* challenge was to ensure chemical purity. This was rendered dif cult by one of the characteristic features of nanoparticles, namely their immense surface area: on a weight-by-weight basis, their external surface is several million times larger than that of a human being: 1 g of 30 nm diameter nanoparticles has an external surface area larger than the combined surface areas of one hundred human beings. In addition, the transporter molecule HSA offers binding sites for hundreds of small molecules, and this, combined with the huge surface area of the particles rendered it dif cult to obtain clean particles as a product. Finally, one of the constituents essential for creating these nanoparticles, gadolinium, is highly toxic in non-chelated form. Our transchelation data based on the release of "free" radionuclide from ^{111}In-labelled nanoparticles indicated that the chelate would release free metal into the living tissues at signi cant rates. Recent FDA alerts concerning serious disease after off-license application of gadolinium chelates in people with kidney illnesses have been well publicised in the literature (Broome et al. 2007; Kuo et al. 2007; Rinck 2008; Rofsky et al. 2008; Sadowski et al. 2007). The edgling eld of nanomedicine is developing concepts and techniques of "nanotoxicology" (Debbage and Jaschke 2008), and aims to avoid or minimise any exposure of animals or humans to toxins, so exposure to non-chelated Gd released from nanoparticles must be carefully de ned, to permit later adjustments to the nanoparticle formulation.

These considerations of batch size, purity and non-toxicity set the agenda for characterising the nanoparticles. They

will be followed up later in this discussion. Next, however, we consider the *third* challenge, of measuring the particles and demonstrating that they were in fact nanoparticles and not, for example, microparticles. This is especially important for nanoparticles destined for use in living tissues, which contain many structures of nanometer size, and in which size may determine the outcome of interactions within the tissue. The immense surface area of nanoparticles varies with the square of the nanoparticle diameter (surface area of a sphere $= 4\pi r^2$), and since many essential functions of nanoparticles depend quantitatively on chemical groups decorating the nanoparticle surface, nanoparticle size should be standardised so far as possible. At the present state of technical development, the size of the nanoparticles provides the only possibility of calculating the composition of the nanoparticles. Since nanoparticle size is a statistical property - the average size within a batch—its description should always include both the mean value and a measure of size variation, such as either standard deviation (SD), coef cient of variation (CV), or polydispersity index (PDI) (these are all related mathematically to one another).

Direct visualisation of nanoparticles, producing an image which can be measured by use of a ruler, requires optical magni cation of at least [10 mm/100 nm] 100,000×. Electron microscopy is therefore an essential tool in development of nanoparticles. Three possible preparative techniques are available for transmission electron microscopy (TEM), namely xation followed by embedding in plastic such as epon, or rapid freezing followed by preparation of ultrathin frozen sections, or negative contrast imaging of dried-down nanoparticle suspensions. Whereas the most accurate measurements might be expected from ultracryotomy, this method also involves the greatest preparative effort. We selected negative contrast TEM because it is rapid, and we were able to demonstrate (Fig. 4) that it provided an accurate assessment of the size of HSA molecules, in the 5–15 nm size range, in good agreement with the 3 × 8 × 8 nm dimensions of the molecule as determined by X-ray diffraction analyses (Curry et al. 1998; Sugio et al. 1999). This rapid and simple method could therefore be trusted to provide accurate data for nanoparticles in the 20–100 nm size range. The results were TEM images (Figs. 4, 7), acquired at ×100,000 magni cation, showing hundreds of nanoparticles simultaneously, with size variability detectable at a glance. To quantify size and variability of nanoparticle populations by use of TEM we adapted concepts familiar in polymer chemistry. A particle population can be considered as an ensemble of particles of discrete sizes, each particle having a mass M described by a whole number from the list $[i = 1 \rightarrow \infty]$, and written as M_i, for example, $M_i = 10{,}000$ Daltons. The variability of this population can be described by comparing two different types of average size values. The rst of these ($\overline{M_W}$) is the average weighted according to particle masses. The second ($\overline{M_N}$) is the average M_i weighted according to particle numbers. In polymer chemistry, the calculation uses molecular *masses*, which are easily measured. Our calculations however were based on morphological data, in which particle *volumes* are easily measured. We therefore used the same equations as in polymer chemistry, but replaced the symbol M (for "mass") with the symbol V (for "volume"). We also replaced the symbol w (for "weight") with v (for "volume"). The result of the calculation is the same because volume and mass relate directly to one another (mass = volume × density, and we assume all the particles in the population have the same density). To analyse our morphological data, we therefore wrote $\overline{V_V}$ for the size average based on particle volumes and $\overline{V_N}$ for the size average based on particle numbers. Adapting the equations, the average based on particle volumes is calculated as $\overline{V_V} = \sum_{i=1}^{\infty} v_i V_i$, where $v_i = \frac{N_i V_i}{\sum_{i=1}^{\infty} N_i V_i}$. The average based on particle numbers is calculated as $\overline{V_N} = \frac{\sum_{i=1}^{\infty} N_i V_i}{\sum_{i=1}^{\infty} N_i}$. In these formulae, the subset of particles having the volume "m^3, *for example all particles with volume* $i = 10{,}000\ nm^3$", is listed as V_i, N_i is the number of the nanoparticles listed in this subset V_i, $N_i V_i$ is the total volume of all the nanoparticles in this subset V_i. Therefore, v_i represents the total volume of the particles in subset V_i as a fraction of the total volume of the particles in the entire particle population. In polymer chemistry, the quotient $\frac{\overline{M_W}}{\overline{M_N}}$ gives the ratio of the half-width at half height to the average value of the (bell-shaped) size distribution, which is known as the polydispersity index (PDI). In our adapted calculations the equivalent is PDI $= \frac{\overline{V_V}}{\overline{V_N}}$. Observe in the above equations for $\overline{V_V}$ and $\overline{V_N}$ that only nanoparticle volumes and numbers need to be assessed: if we possess a list showing the volume of each particle in the population, we can sort it into sublists, one for each sizeband, and from these sublists we can calculate both the average particle size and the PDI. This list is easily obtained: since the projection and cross-sectional areas of each (spheroidal) particle in the TEM image may be considered as equal (i.e. the EM delivers an accurate image), then the volume of each particle is easily calculated (area $= 4\pi r^2$ and volume $= (4/3)\pi r^3$). The uneven edges of our particles hindered automatic thresholding, so we de ned particle edges manually, which limited the number of particles that could be counted to 1,000. However, the remainder of the calculation was automated in a spreadsheet program, and delivered both the average size of the particles and their PDI. This method is de nitive: for any given batch of nanoparticles, the true

average particle size and its variability can be obtained by measuring all the particles (though this would need millions of years to complete). For more detailed consideration of how size variation is calculated and expressed in this work, see the Supplementary Information.

We also employed PCS. The PCS technique stands in strong contrast to the TEM technique, in several respects. The first is its rapidity. Within 5–15 min of placing the nanoparticle suspension in the machine, a size range and an indication of multimodality is presented, the results being obtained from an automated measurement. Second, the underlying theory is much more complex. Whereas TEM bases on counting and measuring easily verifiable individual particle sizes, PCS involves a wide range of different physical variables, none of them easily checked, and some of them entering the subsequent calculation only as approximations. The multi-step and inverse nature of the calculations involved render the result critically dependent on the accuracy of the input data (including the approximations), and for multimodal particle populations an element of modelling is involved, because a multimodal population will not generally give a true Gaussian distribution capable of direct analysis. PCS as a light-scattering measurement depends on particle mass rather than particle number, and therefore yields $\overline{M_W}$ (whereas TEM yields PDI $= \frac{\overline{V_V}}{\overline{V_N}} \equiv \frac{\overline{M_W}}{\overline{M_N}}$). Third, PCS acquires data from immense numbers ($\sim 10^{15}$/ml) of particles, unlike TEM, which with reasonable input of time and effort derives size and PDI data from $\leq 10^3$ particles. In view of the critical sensitivity of PCS size measurements to a wide range of parameters, PCS size data are considerably less accurate and robust than the data derived from TEM, particularly if measurements of calibrated particles are not included. For more detailed analysis of this topic, see the Supplementary Information. Close study of our results showed that careful TEM measurements determined the average size of 30 nm diameter particles to an accuracy of 2 or 3 nm. PCS cannot approach this precision even if care is taken to include calibration measurements. The commonly used presentation of PCS data in the form of peak size averages stated to 0.1 nm ignores the numerous sources of inaccuracy and claims that PCS measures to a precision of 0.3%. This illusion of PCS accuracy is easily dispelled by checking the CV of the measurements. Interestingly, this is a much more robust measurement than the size measurement, because it is derived directly from the value for the characteristic decay time ($\Gamma = \tau/2$) of the autocorrelation: PDI $= \sqrt{\frac{\left\{\left(\Gamma - \overline{\Gamma}\right)^2\right\}}{\Gamma^2}}$, where the curly brackets denote an average over a distribution of decay times (Chang et al. 1982). Its accuracy therefore does not depend on knowledge of the values of several physical parameters). In our future work, we will state PCS results to a similar degree of accuracy as the TEM data, that is, 2–3 nm. Furthermore, for PCS we will state the PDI derived from the Gaussian CV measurement and not from the modelled individual peak distribution, which in our experience gave values which were unrealistically low and bore no relationship to the TEM results. We found rapid PCS measurements useful in monitoring syntheses: significant deviations from the expected size served to indicate that synthesis was not proceeding as planned (for example see the four problem batches illustrated in Fig. 5). This utility of PCS however, was available only in the hands of an experienced operator. In those experienced hands, sizes measured by PCS differed by a factor up to 5× in approximately 10% of measurements (see Fig. 6), a proportion which improved as the operator became familiar with the nanoparticles being measured.

In our work interbatch variability extended from PDI = 1 to PDI = 2.5. The PCS data clustered between PDI = 1.3–1.6; the absence of similar clustering in the TEM data might be due to the smaller number of batches studied by TEM. Both PCS and TEM revealed the significant interbatch variability obtained by using a standardised synthesis protocol and both methods demonstrated the same range of variability: PDI = 1–2.5. This agreement concerning size variation was found in spite of the entirely different approaches involved in these two techniques. Note that the TEM measurements were calculated directly as PDI, whereas PCS measurements were based on direct measurements of CV. Note that the absolute sizes measured by TEM and those modelled by PCS are expected to differ, because TEM of negatively contrasted nanoparticles measures the protein material comprising the bulk of the nanoparticles, whereas PCS measures the hydrodynamic diameters of the particles, which vary according to the solute and its concentration (Cormode et al. 2009).

In addition to routine negative contrast assessments using TEM, we also carried out comparisons with Epon-embedded nanoparticles, because later pharmacokinetic studies will visualise nanoparticles interacting with tissues, and these will be Epon-embedded. The sizes measured for nanoparticles in negative contrast TEM and for those embedded in Epon sections were closely similar (Fig. 7). In subsequent work, we are therefore confident that nanoparticles in Epon-embedded tissues will be visualised at their correct size. Since the two TEM procedures give similar results, we generally used negative contrast TEM because it involves much less preparatory work. Epon embedment of nanoparticles can however lead to spurious results, because osmium tetroxide mixed with alcohol occulates in the form of nanoparticles, generally ~200 nm diameter (Fig. 7). Precautions against this involve adequate rinsing of nanoparticle suspensions, and

familiarity with the appearance of the osmium nanoparticles.

As shown in Fig. 6, both TEM and PCS showed numerous batches to have nanoparticle average diameters between 15–20 nm. A smaller number of batches had nanoparticle average diameters ~35 nm. In Table 1, we present data and calculations showing that the smaller nanoparticles (~20 nm diameter) each contained 11–19 HSA molecules, and bore 200–350 Gd ions. The larger nanoparticles (~30 nm diameter) each contained ~30–60 HSA molecules and bore ~680–1,200 Gd ions. Since the advantages associated with nanoparticle formulations are greater for the larger nanoparticles (more signal amplification, better targeting efficiency), the larger nanoparticles are to be preferred unless they cause mechanical damage or exhibit enhanced toxicity. As noted above, we did observe mechanical damage to endothelial cells caused by nanoparticles of 400 nm diameter (Paschkunova-Martic et al. 2005), but we have never observed such damage caused by nanoparticles smaller than 100 nm diameter. Data presented in this paper showed that none of the batches tested showed cytotoxicity. In view of these data, we selected 35 nm as the preferred or "correct" size for our nanoparticles, and in later work (manuscript in preparation), we achieved highly standardised series of batches containing nanoparticles of average size 35 nm.

One of our objectives being to prepare nanoparticles which can be loaded with drug molecules, we based this work on the body's natural transport protein, albumin. Although at this stage we did not load the nanoparticles, we aimed to maintain the albumin in a configuration capable of being loaded; ideally, the nanoparticles should be capable of loading themselves with a drug simply by immersion in a solution of that drug. The two major binding sites of albumin (Curry et al. 1998, 1999) should therefore remain in native configuration in the nanoparticles, retaining the slight flexibility of the molecule which HSA needs for specific binding (Carter and Ho 1994; Spector 1975; Stewart et al. 2003; Sugio et al. 1999). We obtained preliminary evidence that the HSA in our nanoparticles had retained its native tertiary configuration, namely that antigenic epitopes characteristic of HSA were present on and in the nanoparticles. The positive evidence for this was obtained by use of both monoclonal and polyclonal antibodies. We did not proceed at this stage to conclusive proof that the HSA within the particles can be loaded with a ligand.

The nanoparticles were composed of ~95% HSA–DTPA–Gd conjugates, but how many conjugate molecules were contained within each particle? This, in turn, determined the number of Gd ions present within each particle, and therefore was a major factor in determining the relaxivity of the nanoparticles. Since we had measured the nanoparticle sizes quite accurately, we could calculate the number of HSA–DTPA–Gd conjugates able to fit into the volume of one nanoparticle. For this, the volume of the conjugates must be known. HSA is a heart-shaped molecule, which Sugio et al. (1999) state to have an approximate size 80 × 80 × 30 Å. At first sight, this suggests an approximate volume of 192 nm^3, but measurements of the images they present show that the volume is actually between 85 and 105 nm^3, our calculations in the "Results" of this paper are based on a volume of 90 nm^3. The true number of conjugates fitting into one nanoparticle is less than this result however, because they are not packed so tightly that they occupy the entire volume of the nanoparticle. The packing density of regularly shaped bodies has been the topic of mathematical investigation since classical times, became a popular modern topic as problem 18 in Hilbert's list (Reid 1996; Rowe and Gray 2000; Weyl 1944) and is today still at the cutting edge of mathematical research (Torquato and Jiao 2009). Packing densities are stated as particle volume fraction of the "fundamental cell" containing the centroid of one particle. Geometrically, maximum packing densities close to 0.35 represent low values for regular polyhedra (Hoylman 1970; Torquato and Jiao 2009). For centrally symmetric regular solids (octahedron, dodecahedron, icosahedron), extremely high packing densities (up to 0.947) can be achieved (Minkowski 1904), but this is due to their central symmetry. For all other regular polyhedra (lacking central symmetry), the highest possible packing densities are close to the maximal packing density of spheres, which is 0.7408. (Torquato and Jiao 2009). Maximum packing densities of regular solid bodies which are in contact with one another therefore generally lie between 0.35 and 0.75. Albumin molecules are not regular solid bodies, but instead resemble flattened ellipsoids or lozenges, and therefore might be considered to resemble thick tiles rather than regular polyhedra. Packing densities for ellipsoids can be high, exceeding the optimal sphere packing density of 0.7408 (Donev et al. 2004). Indeed, under the extreme conditions leading to crystallisation, albumin molecules form pairs aligned in opposite directions to occupy the asymmetric unit cell of the triclinic crystal lattice (Sugio et al. 1999). In our nanoparticle preparations, such extreme conditions are not present and the association between the molecules is much looser, as shown in the TEM images (Fig. 7). It is likely that important geometric constraints are loosened under these conditions, for example it is not likely that each albumin molecule is touching its partners. Electrical charge effects will play a role in albumin packing in the nanoparticles: a repellent effect amongst similarly charged molecules is likely to reduce packing density in the nanoparticles. Our TEM analysis indicated that the nanoparticles had packing densities δ between 0.35 and 0.45, rather looser than the

geometrical considerations would suggest. However, this technique involved thresholding choices implemented on images of intrinsically low contrast, which called into question the reliability of the data obtained. In order to orient our calculations by reference to other biological systems, we therefore calculated from published data the apparent average packing density of the atoms in a well-characterised biological nanoparticle, the nuclear pore complex, which has a diameter 98 nm, a channel width ~35 nm and a depth ~40 nm (Alber et al. 2007a, b). The calculation showed that this large multi-subassembly natural nanoparticle has an average packing density $\delta = 0.23$, approximately 70% of the lowest value calculated from purely geometrical considerations. Thus, even although we know the sizes of our nanoparticles with some precision, uncertainty in the exact value for their packing density imports an uncertainty into their estimated masses (up to ±30%). In turn, this imports uncertainty into the estimates of their relaxivities. To take account of this uncertainty, we show in Table 1 the nanoparticle masses as calculated using both values of packing density ($\delta = 0.23$ and $\delta = 0.40$). The other parameter in our calculation which might exhibit some uncertainty was the average density of the protein (Quillin and Matthews 2000), but as noted below we obtained measurements in related work indicating that the value we used for this was close to the true value.

The number of Gd ions per nanoparticle is easy to measure, in principle. We attempted to do this by counting the numbers of nanoparticles in a known volume of suspension of known nanoparticle concentration, and measured the concentration of Gd in this suspension by atomic absorption spectrometry. The results that we calculated from these data were approximately ×20 higher than the theoretical maximum. A closer look showed that the error arose from the uneven distribution of nanoparticles in the dried-down droplets on the EM grids. Most of the nanoparticles dry down at the rim of the droplet, where they form dense masses that cannot be counted. In the droplet middle, where counting is possible, there are relatively few particles and therefore the calculated Gd:particle ratios are (20×) too high. The inaccuracies associated with this direct measurement were larger than those associated with the size/mass calculations presented above. For this reason, we omitted this data from the "Results"; we are modifying the methodology used in future work to count the nanoparticles because this type of direct count will be of high value if it can be made reliable.

To determine the relaxivities of conjugates and nanoparticles required, at least five different types of measurement, namely the molecular weight of the conjugates and diameters of the nanoparticles, the density of the nanoparticles, the content of Gd in both conjugates and nanoparticles, the content of HSA in both conjugates and nanoparticles, and the relaxation rates R_1 and R_2 of the conjugates and the nanoparticles in MRI. All except one of these measurements (density) were carried out during this work; density measurements made on other albumin-based materials (manuscript in preparation) produced reliable and constant values in close agreement with results stated for albumin microspheres by earlier authors (MacAdam et al. 1997), and in general agreement with theoretical values (Quillin and Matthews 2000), therefore, these values were inserted into the calculations here. Taken together, our data indicated that our nanoparticles were 20–30 nm in size, with intrabatch PDI 1.2–1.4, and with some indications that interbatch variation was generally due to the presence of contaminating educts or of nanoparticle aggregation. Assuming their mass density to be 1.4 g/cm^3, and their molecular packing density to be 0.4, the particles in different batches had masses varying between 1–6 MDa, were in the different batches composed of 25–75 molecules of naturally con gured HSA, and bore 500–1,500 Gd ions (details in Table 1). This was the essential information necessary to consider the MR imaging properties of the nanoparticles. The several types of data produced by the measurements were combined in a series of calculations to yield, successively, values for relaxation rates, relaxivities per particle and nally, relaxivities per Gd ion within the particles. The results of this series of calculations are presented in Table 1. As evident from the Table 1, the conjugates exhibit higher r_1 and r_2 values per Gd ion than is found in the simple DTPA–Gd chelates. This size-related increase of r_1 and r_2 per Gd ion was described by earlier authors (Brasch 1991; Ogan et al. 1987); the value we calculated (~6,000/Ms) is smaller than would be expected from those earlier reports (~14,000/Ms). Several possible explanations can be considered for this. One is the purity of the nanoparticle preparations, for example, contaminating educts may remain in the preparations, or some nanoparticles might disintegrate into their component conjugate molecules; either of these possibilities would increase the number of extremely small Gd-bearing structures in the nanoparticle suspension and thus reduce the observed (average) relaxivity per Gd ion. A different type of consideration is the exchange correlation time of protons in our nanoparticles: the increase in relaxivity we observed at raised temperatures would support that this is the limiting factor for their relaxivity (Laurent et al. 2004). In this connection, as noted above, the relaxivities per Gd ion are larger in larger structures. We found no evidence for this in relation to the nanoparticles: their relaxivity per Gd ion was not higher than in the conjugates, although the nanoparticles were hundreds of times larger than the conjugates. We offer as explanation for this that the nanoparticles may not possess suf cient internal connectivity and rigidity for this

size-dependent increase of relaxivity to become manifest. As a final point in connection with measurement of nanoparticle relaxivities, we consider the synthesis standardisation. By combining data from numerous batches, we were able to determine the range of relaxivities observed in the nanoparticles, but not always to quantify the exact values for each of a series of batches; the variability amongst the batches precluded statement of precise standardised values. It is, however, essential to achieve standardised results for later pharmaceutical applications, and this motivates further work to understand the sources of the variability (manuscript in preparation).

The surface charge of the nanoparticles, measured as zeta potential, is sufficient to repel neighbouring nanoparticles and so hold the suspension in the form of individual particles. This is seen clearly in images such as Fig. 4c and Fig. 7d. A suspension of charged individual particles retains the characteristic features of the nano-size scale, for example, the enormous surface area. In contrast, particles with little charge may clump into aggregates, which have the same total mass as the nanoparticle suspension but have a strongly reduced surface area. Such aggregated forms cannot be provided with targeting capability by attachment of a few targeting groups, and they enter into interactions with living tissues which are very different to those observed for individual nanoparticles. The surface charge on the nanoparticles therefore has an important function in maintaining the nanoscale features of nanoparticle suspensions. At neutral pH, the HSA-DTPA conjugates bear a negative charge, which is neutralised when Gd^{3+} ions are chelated in the DTPA groups; the HSA–DTPA–Gd conjugates therefore bear little charge. The nanoparticles created from the HSA–DTPA–Gd conjugates bear a charge which is usually close to −40 mV; we consider this negative charge arises from the presence of PLA within the particles.

Examination of the stability of the nanoparticles and of their components was a high priority in this work, because we planned follow-up studies of particle pharmacokinetics in animal models. The first question related to potential gadolinium metal toxicity, for reasons noted above, and this depended on the stability of the DTPA chelation that was used. Metal chelates slowly transmetallated, the original metal (e.g. Gd^{3+}) being replaced by a different metal (e.g. Fe^{3+}), thus exiting the organic chelating cage to become free (and potentially toxic) in the surrounding water. Although equilibrium constants for the binding of Gd to chelators are extremely high as measured in water or buffers, the amounts of Gd released in blood serum are several orders of magnitude greater than predicted by these stability constants. This is because the fluid environment of the blood and of tissues exerts strong destabilising effects on DTPA chelates, especially if phosphate (Frenzel et al. 2008) or free iron (Kunnemeyer et al. 2009) is present. It is technically an involved procedure to measure Gd loss rates from DTPA chelates; techniques such as mass spectrometry are required (Kunnemeyer et al. 2009). Within this study, we investigated the chelate stability by use of the trivalent radiometal ^{111}In. In analysing the radiolabelled nanoparticles after incubation in a range of physiologically relevant fluids by instant thin layer chromatography and electronic autoradiography. We found that the ^{111}In-content of radiolabelled nanoparticles suspended in blood plasma decreased by as much as 14% in 24 h, a result comparable to that found by Arano et al. (1996). In vivo, however, a higher dechelation rate as well as possible transmetallation to other endogenously available metal ions can be expected (Kunnemeyer et al. 2009). During the 1990s, it became clear that linear chelates such as DTPA–Gd released Gd relatively rapidly into body tissues, the presence of free Gd becoming measurable in the tissues of experimental animals within 60 min (Tweedle 1992; Wedeking et al. 1992), with significant fractions of initial Gd dose found in bone at 24 h (Harrison et al. 1993). Much later, similar data were collected for human patients (Gibby et al. 2004; White et al. 2006). This relatively rapid dechelation in vivo could not be reconciled with the high thermodynamic stability of the chelates, according to which equilibration at neutral pH would require several years. Recent work resolved the question by pointing out that kinetic stability (dissociation rate) of the chelates is more relevant in the situation within living tissues. This more recent literature has been comprehensively reviewed by Port et al. (2008). The rate of dechelation of Gd–DTPA chelates is stated in the newer literature as similar to that which we found for In-DTPA chelates (Laurent et al. 2006). It is a consequence of these considerations that nanoparticle breakdown products remaining within the organism would release their gadolinium, the residual Gd concentration falling to <1% of the initial dose only after approximately 6 weeks, having leaked free gadolinium into the body fluids during this time. These high rates of Gd release in blood serum may make it necessary to employ different types of chelating ligands in formulation of nanoparticles in future work, for example, macrocyclic chelators which release almost no Gd in the blood serum environment (Frenzel et al. 2008; Port et al. 2008).

The planned application of the nanoparticles involves injection into the bloodstream. This exposes the particles to a heated, turbulent, enzyme-rich fluid in which shear forces, friction and mechanical disruption amongst colliding blood cells all threaten to disintegrate the particles. Nanoparticles for use in MRI should be tested for their stability under conditions relevant to those encountered in the blood circulation. We therefore tested the particles in vitro to determine their resistance to destruction, and also

their modes of breakdown. The particles were found to be stable to the stressors expected in the blood circulation of an animal (turbulence, temperature, and attack by agents present in the blood), so they could be expected to retain their integrity under the conditions encountered in blood owing through large blood vessels. The disruption of the nanoparticles by SDS detergent is expected to occur because SDS unfolds the structure of the component HSA molecules (Pallansch and Briggs 1954) and therefore unravels the fundamental structural matrix of the nanoparticles.

In vitro testing of the nanoparticles to study their potential toxic effects on cells indicated that these particles are non-cytotoxic in a hierarchical screening system. Two tests (MTS and ATP-content), designed specifically to assay nanoparticle cytotoxicity, showed that the nanoparticles did not disrupt cellular metabolism. The LDH release assay showed that they did not disrupt cellular membranes. A further step of testing assayed toxic and immunological effects of the nanoparticles in the blood. The particles did not cause lysis of red blood cells. They did not activate clotting mechanisms and they did not activate the complement system to trigger immune responses. These results suggest strongly that it is safe to introduce these nanoparticles into the bloodstream of test animals. In further rounds of nanoparticle development, the nanoparticles will be subjected to more intensive testing (higher concentrations of nanoparticles incubated with the cells for longer periods of time), coordinated with the pharmacokinetic studies of the particles (manuscript in preparation).

The HSA-based nanoparticles thus far appear well suited for potential application in animals. In this case, economic and logistical considerations come to the fore. The first of these is the amount that can be prepared. The batch sizes reported here are a few grams. These are sufficient for testing in laboratory animals, for example testing in a rabbit requires an estimated 300 mg. Upscaling to kilogram batches is possible at the laboratory scale by "numbering up", i.e. parallel batch production. Industrial experience with albumin-based preparations began in the era 1940–1950 (Gonzalez and Kanneworff 1998; Roberts and Bratton 1998), and the recent availability of albumin-based nanoparticulate therapeutic agents (eg: Abraxane®) shows that the logistical chain can be established for albumin-containing particles. However, each particle formulation requires consideration on its own merits. The costs of preparing the particles described here are a few euros per gram and upscaling to kilograms is possible.

For which applications are these particles suitable? They are designed to circulate in the bloodstream, producing a strong signal in MRI. Some uptake into vascular endothelial cells, for example via SPARC receptors, is likely. Uptake by macrophages must be expected, and albumin-based particles could possibly enter the renal uptake and recycling system for albumin. To modulate these interactions, the particles require surface decorations such as attachment of PEG or sialic acids, in order to utilise general charge interactions, or to exploit stereospecific interactions. Each of the 150 albumin molecules within the particle bears 19–30 amino groups of varying reactivity at or near the molecule's surface (Goldfarb 1956) and 21 carboxyl groups at the molecule's surface (Weber et al. 2000a, b). Measurements made on albumin microspheres have shown the presence of several thousand each of amino and carboxyl groups per μm^2 at the surfaces of aldehyde-cross-linked 10–26 μm diameter albumin microspheres (MacAdam et al. 1997). There is, therefore, wide scope for decorating the nanoparticles. However, each new architecture attached to the particle surface will alter the biology, toxicology, immunology and the pharmacokinetics of the particle. Each such alteration necessitates a fresh round of exploring and documentation of the new particle properties. At present, our characterisation of these particles satisfies 18 of the 55 requirements listed by the Organisation for Economic Co-operation and Development (OECD 2008). Since the OECD list applies to each freshly decorated particle formulation, the urgent need for rapid assays in nanoparticle development becomes obvious. The following remarks should therefore be seen in terms of possibilities, and not as a program that can be realised in a brief span of years. Albumin-based nanoparticles provide a platform ideally suited as carrier for an extremely wide range of drugs. To this platform can be attached thousands of modulatory and functional groups to regulate interactions with molecules in the blood and upon cells, and to navigate the particles into target sites for accumulation there. This nanoparticle platform is well suited to carry out the aims set forth in the EU Strategic Research Agenda (Boisseau et al. 2006). Amongst other things, it is suitable for providing a series of histochemical reagents that can be used for imaging specific molecules in living animals. Our first steps towards this show the promise of this approach (manuscript in preparation).

The aim of our work is to develop a "stain" in the classical histological sense, but one which can be employed to generate image contrast within specific structures and tissues *within living organisms*, animal or human. This extends classical histochemistry by applying its concepts and methods to living tissues in intact organisms, and the use of apparatus other than microscopes. The development of the staining reagent will pass through the same stages, as did familiar staining reagents used in microscopy, but with extra steps for clinical applications because this reagent will be subject to regulations controlling production of pharmaceutical agents designed for use in human subjects. In addition, an albumin-based reagent capable of providing

speci c contrast in radiology imaging systems will also be suitable for loading with drugs and therefore capable of use in both diagnostics and therapy. Following our earlier proof of principle (Paschkunova-Martic et al. 2005), this paper describes our rst step in developing a staining reagent for providing speci c contrast in clinical MRI, an imaging modality of the greatest clinical value. This paper is the rst in a series, in which we start from rst principles and develop the staining reagent "from the ground up". We have shown here that standardising the synthesis protocol does not lead to a standardised product; data feedback at several steps during the synthesis will be needed, to feed back into control processes and thus enable quality criteria to be met throughout the synthesis process. This forms the topic of our later papers (manuscripts in preparation).

Acknowledgments The Austrian Nano-Initiative co- nanced this work as part of the Nano-Health project. The Austrian National Bank Jubilee Program supported this work repeatedly (Projects 9273, 10844, 11574 and 13096).

References

Alber F, Dokudovskaya S, Veenhoff LM, Zhang W, Kipper J, Devos D, Suprapto A, Karni-Schmidt O, Williams R, Chait BT, Rout MP, Sali A (2007a) Determining the architectures of macromolecular assemblies. Nature 450:683–694

Alber F, Dokudovskaya S, Veenhoff LM, Zhang W, Kipper J, Devos D, Suprapto A, Karni-Schmidt O, Williams R, Chait BT, Sali A, Rout MP (2007b) The molecular architecture of the nuclear pore complex. Nature 450:695–701

Andersen-Berg WT, Strand M, Lempert TE, Rosenbaum AE, Joseph PM (1986) Nuclear magnetic resonance and gamma camera tumor imaging using gadolinium-labeled monoclonal antibodies. J Nucl Medicine 27:829–833

Anderson SA, Rader RK, Westlin WF, Null C, Jackson D, Lanza GM, Wickline SA, Kotyk JJ (2000) Magnetic resonance contrast enhancement of neovasculature with alpha(v)beta(3)-targeted nanoparticles. Magn Reson Med 44:433–439

Arano Y, Uezono T, Akizawa H, Ono M, Wakisaka K, Nakayama M, Sakahara H, Konishi J, Yokoyama A (1996) Reassessment of diethylenetriaminepentaacetic acid (DTPA) as a chelating agent for indium-111 labeling of polypeptides using a newly synthesized monoreactive DTPA derivative. J Med Chem 39:3451–3460

Baranov AN, Vlasova IM, Saletskii AM (2004) Investigation of serum-albumin aggregation. J Appl Spectroscopy 71:222–226

Barratt GM (2000) Therapeutic applications of colloidal drug carriers. Pharm Sci Technol Today 3:163–171

Bazile DV, Ropert C, Huve P, Verrecchia T, Marlard M, Frydman A, Veillard M, Spenlehauer G (1992) Body distribution of fully biodegradable [14C]-poly(lactic acid) nanoparticles coated with albumin after parenteral administration to rats. Biomaterials 13:1093–1102

Behrens PQ, Spiekerman AM, Brown JR (1975) Structure of human serum albumin. Fed Proc Fed Am Soc Exp Biol 34:591 abstr. 2106

Blanco-Prieto MJ, Campanero MA, Besseghir K, Heimgartner F, Gander B (2004) Importance of single or blended polymer types for controlled in vitro release and plasma levels of a somatostatin analogue entrapped in PLA/PLGA microspheres. J Control Release 96:437–448

Boisseau P, Kiparissides C, Pavesio A, Saxl O, Ambrosio L, Benninghofen A, Bigay C-N, Borros S, Briel A, Bruce D, Chabbal J, Charbit F, Coche T, Deacon J, Debbage P, Eaton M, Fuchs H, Fuhr G, Goossens J, Guenther R, Hawlina M, Hofmeister A, Kasemo B, Kirkpatrick J, Kuhn MH, Marche P, Meisel HJ, Mestais C, Moore R, Ogorevc B, Peponnet C, Pieber T, Pirovano D, Puget P, Reinmann M, Riese J, Rodriguez JR, Samitier J, Scher er H, Schild C, Schmidt S, Schreder S, Souquet J, Subramaniam V, Tavitian B, Venturini P, Vericat JA, von Bally G, Weltring K-M, Williams D, Zivin M (2006) European technology platform on nanomedicine: nanotechnology for health—strategic research agenda. European Commission, Of ce for Of cial Publications of the European Communities (Luxembourg), 39 p. ISBN 92-79-02203-2

Boury F, Marchais H, Proust JE, Benoit JP (1997) Bovine serum albumin release from poly(hydroxy acid) microspheres: effects of polymer molecular weight and surface properties. J Control Release 45:75–86

Brasch RC (1991) Rationale and applications for macromolecular Gd-based contrast agents. Magn Reson Med 22:282–287

Broome DR, Girguis MS, Baron PW, Cottrell AC, Kjellin I, Kirk GA (2007) Gadodiamide-associated nephrogenic systemic brosis: why radiologists should be concerned. Am J Roentgenol 188:586–592

Brown JR (1975) Structure of bovine serum albumin. Fed Proc 34:591

Carter DC, Ho JX (1994) Structure of serum albumin. Adv Protein Chem 45:153–203

Chang EL, Gaber BP, Sheridan JP (1982) Photon correlation spectroscopy study on the stability of small unilamellar DPPC vesicles. Biophys J 39:197–201

Chu B (1974) Laser light scattering. Academic Press Inc, New York

Chu B, Gulari E, Gulari E (1979) Photon correlation measurements of colloidal size distributions. II. Details of histogram approach and comparison of methods of data analysis. Physica Script 19:476–485

Chuang VTG, Otagiri M (2007) Recombinant human serum albumin. Drugs Today 43:547–561

Cochrane Injuries Group Albumin Reviewers (1998) Human albumin administration in critically ill patients: systematic review of randomised controlled trials. BMJ 317:235–240

Colgan K, Moody ML, Witte K (2000) Responsible use of blood products in response to supply and demand. Am J Health System Pharm 57:2094–2098

Collidge TA, Thomson PC, Mark PB, Traynor JP, Jardine AG, Morris STW, Simpson K, Roditi GH (2007) Gadolinium-enhanced MR imaging and nephrogenic systemic brosis: retrospective study of a renal replacement therapy cohort. Radiology 245:168–175

Cooper MS, Sabbah E, Mather SJ (2006) Conjugation of chelating agents to proteins and radiolabeling with trivalent metallic isotopes. Nat Protoc 1:314–317

Cormode DP, Skajaa T, Fayad ZA, Mulder WJM (2009) Nanotechnology in medical imaging: probe design and applications. J Am Heart Assoc 29:992–1000

Cowper SE, Robin HS, Steinberg SM, Su LD, Gupta S, LeBoit PE (2000) Scleromyxoedema-like cutaneous diseases in renal-dialysis patients. Lancet 356:1000–1001

Cowper SE, Kuo PH, Bucala R (2007) Nephrogeneic systemic brosis and gadolinium exposure: association and lessons for idiopathic brosing disorders. Arthritis Rheum 56:3173–3175

Cregg JM, Cereghino JL, Shi J, Higgins DR (2000) Recombinant protein expression in *Pichia pastoris*. Mol Biotechnol 16:23–52

Curry S, Mandelkow H, Brick P, Franks N (1998) Crystal structure of human serum albumin complexed with fatty acid reveals an asymmetric distribution of binding sites. Nature Struct Biol 5:827–835

Curry S, Brick P, Franks NP (1999) Fatty acid binding to human serum albumin: new insights from crystallographic studies. Biochem Biophys Acta 1441:131–140

Daldrup-Link HE, Brasch RC (2003) Macromolecular contrast agents for MR mammography: current status. Eur Radiol 13:354–365

Debbage P (2009) Targeted drugs and nanomedicine: present and future. Curr Pharm Des 15:153–172

Debbage P, Jaschke W (2008) Molecular imaging with nanoparticles: giant roles for dwarf actors. Histochem Cell Biol 130:845–875

Donev A, Stillinger FH, Chaikin PM, Torquato S (2004) Unusually dense crystal ellipsoid packings. Phys Rev Lett 92:1–255506

Dugiaczyk A, Law SW, Dennison OE (1982) Nucleotide sequence and the encoded amino acids of human serum albumin mRNA. Proc Natl Acad Sci USA 79:71–75

Edgell CJ, McDonald CC, Graham JB (1983) Permanent cell line expressing human factor VIII-related antigen established by hybridization. Proc Natl Acad Sci USA 80:3734–3737

Enochs WS, Harsh G, Hochberg F, Weissleder R (1999) Improved delineation of human brain tumors on MR images using a long-circulating, superparamagnetic iron oxide agent. J Magn Reson Imaging 9:228–232

Erstad BL (1996) Viral infectivity of albumin and plasma protein fraction. Pharmacotherapy 16:996–1001

Farooki A, Narra V, Brown J (2004) Gadofosveset. Curr Opin Invest Drugs 5:967–976

Fehske KJ, We Muller, Wollert U (1981) The location of drug binding sites in human serum albumin. Biochem Pharmacol 30:687–692

Finfer S, Bellomo R, Boyce N, French J, Myburgh J, Norton R (2004) The SAFE Study Investigators. A comparison of albumin and saline for uid resuscitation in the intensive care unit. N Eng J Med 350:2247–2256

Flacke S, Fischer S, Scott MJ, Fuhrhop RJ, Allen JS, McLean M, Winter P, Sicard GA, Gaffney PJ, Wickline SA, Lanza GM (2001) Novel contrast agent for molecular imaging of brin. Implications for detecting vulnerable plaques. Circulation 104:1280–1285

Frank PG, Scott EW, Park DS, Lisanti MP (2003) Caveolin, caveolae, and endothelial cell function. Arterioscler Thromb Vasc Biol 23:1161–1168

Frenzel T, Lengsfeld P, Schirmer H, Hauer J, Weinmann H-J (2008) Stability of Gadolinium-based magnetic resonance imaging contrast agents in human serum at 37 Invest Radiol 43:817–828

Frisken BJ (2001) Revisiting the method of cumulants for the analysis of dynamic light-scattering data. Appl Opt 40:4087–4091

Gallo JM, Hung CT, Perrier DG (1984) Analysis of albumin microsphere preparation. Int J Pharm 22:63–74

Gibby WA, Gibby KA, Gibby WA (2004) Comparison of Gd-DTPA-BMA (Omniscan) versus Gd-HP-DO3A (Pro-Hance) retention in human bone tissue by inductively coupled plasma atomic emission spectroscopy. Invest Radiol 39:138–142

Goldfarb AR (1966) Heterogeneity of amino groups in proteins. I. Human serum albumin. Biochemistry 5:2574–2578

Goldwasser P, Feldman J (1997) Association of serum albumin and mortality risk. J Clin Epidemiol 50:693–703

Goll JH, Stock GB (1977) Determination by photon correlation spectroscopy of particle size distributions in lipid vesicle suspensions. Biophys J 19:265–273

Goll J, Carlson FD, Barenholz Y, Litman BJ, Thompson TE (1982) Photon correlation spectroscopic study of the size distribution of phospholipid vesicles. Biophys J 38:7–13

Gonzalez ER, Kannewurf BS (1998) Clinical review of appropriate uses for albumin. US Pharmacist 23:HS15–HS26

Gradishar WJ, Tjulandin S, Davidson N, Shaw H, Desai N, Bhar P et al (2005) Phase III trial of nanoparticle albumin bound paclitaxel compared with polyethylated castor oil-based paclitaxel in women with breast cancer. J Clin Oncol 23:7794–7803

Griffel MI, Kaufman BS (1992) Pharmacology of colloids and crystalloids. Crit Care Clin 8:235–253

Gururaj Rao A, Narasinga Rao MS (1983) Effect of sodium dodecyl sulphate on the high molecular weight protein fraction of mustard (*Brassica juncea*) and rapeseed (*Brassica campestris*). J Biosci 5:301–309

Harrison A, Walker CA, Pereira KA, Parker D, Royle L, Pulukkody K, Norman TJ (1993) Hepato-biliary and renal excretion in mice of charged and neutral gadolinium complexes of cyclic tetra-aza-phosphinic and carboxylic acids. Magn Reson Imaging 11:761–770

Hauff P, Reinhardt M, Briel A, Debus N, Schirner M (2004) Molecular targeting of lymph nodes with L-Selectin ligand-speci c US contrast agent: a feasibility study in mice and dogs. Radiology. doi:10.1148/radiol.2313030425

He XM, Carter DC (1992) Atomic-structure and chemistry of human serum albumin. Nature 358:209–215

Hiemenz PC (1984) Distribution functions. In: Hiemenz PC (ed) Polymer chemistry: the basic concepts. Marcel Dekker, New York. ISBN 082477082X, pp 34ff

Ho JX, Holowachuk EW, Norton EJ, Twigg PD, Carter DC (1993) X-ray and primary structure of horse serum albumin (*Equus caballus*) at 0.27-nm resolution. Eur J Biochem 215:205–212

Hoylman DJ (1970) The densest lattice packing of tetrahedra. Bull Am Math Soc 76:135–137

Ivanov AI, Korolenko EA, Korolik EV, Firsov SP, Zhbankov RG, Marchewka MK, Ratajczak H (2002) Chronic liver and renal diseases differently affect structure of human serum albumin. Arch Biochem Biophys 408:69–77

Johansson LO, Bjørnerud A, Ahlström HK, Ladd DL, Fujii DK (2001) A targeted contrast agent for magnetic resonance imaging of thrombus: implications of spatial resolution. J Magn Res Imag 13:615–618

Kang HW, Josephson L, Petrovsky A, Weissleder R, Bogdanov A Jr (2002) Magnetic resonance imaging of inducible E-selectin expression in human endothelial cell culture. Bioconjugate Chem 13:122–127

Khurana A, Runge VM, Narayanan M, Greene JF Jr, Nickel AE (2007) Nephrogenic systemic brosis. A review of 6 cases temporally related to gadodiamide injection (Omniscan). Invest Radiol 42:139–145

King CP, Li MD, Bednarski MD (2002) Vascular-targeted molecular imaging using functionalized polymerized vesicles. J Magn Res Imag 16:388–393

Koppel DE (1972) Analysis of macromolecular polydispersity in intensity correlation spectroscopy. The method of cumulants. J Chem Phys 57:4814–4820

Kragh-Hansen U (1981) Molecular aspects of ligand binding to serum albumin. Pharmacol Rev 33:17–53

Kramer PA (1974) Albumin microspheres as vehicles for achieving speci city in drug delivery. J Pharm Sci 63:1646–1647

Künnemeyer J, Terborg L, Nowak S, Telgmann L, Tokmak F, Karadurmus BK, Günsel A, Wiesmüller GA, Waldeck J, Bremer C, Karst U (2009) Analysis of the contrast agent Magnevist and its transmetalation products in blood plasma by capillary electrophoresis/electrospray ionization time-of- ight mass spectrometry. Anal Chem 81:3600–3607

Kuo PH, Kanal E, Abu-Alfa AK, Cowper SE (2007) Gadolinium-based MR contrast agents and nephrogenic systemic brosis. Radiology 242:647–649

Langer K, Balthasar S, Vogel V, Dinauer N, von Briesen H, Schubert D (2003) Optimization of the preparation process for human serum albumin (HSA) nanoparticles. Int J Pharm 257:169–180
Lauffer RB, Parmelee DJ, Dunham SU, Ouellet HS, Dolan RP, Witte S, McMurry TJ, Walovitch RC (1998) MS-325: albumin-targeted contrast agent for MR angiography. Radiology 207:529–538
Laurent S, Vander Elst L, Fu Y, Muller RN (2004) Synthesis and physicochemical characterization of Gd-DTPA-B(SA)4, a new MRI contrast agent targeted to in ammation. Bioconjugate Chem 15:99–103
Laurent S, Vander Elst L, Muller RN (2006) Comparative study of the physicochemical properties of six clinical low molecular weight gadolinium contrast agents. Contrast Med Mol Imaging 1:128–137
Lewis JD, Destito G, Zijlstra A, Gonzalez MJ, Quigley JP, Manchester M, Stuhlmann H (2006) Viral nanoparticles as tools for intravital vascular imaging. Nat Med 12:354–360
Liang L, D'Haese PC, Lamberts LV, Van de Vyver FL, De Broe ME (1991) Determination of gadolinium in biological materials using graphite furnace atomic absorption spectrometry with a tantalum boat after solvent extraction. Anal Chem 63:423–427
Lin W, Coombes AGA, Davies MC, Davis SS, Illum L (1993) Preparation of sub-100 nm human serum albumin nanospheres using a pH-coacervation method. J Drug Target 1:237–243
MacAdam AB, Sha ZB, James SL, Marriott C, Martin GP (1997) Preparation of hydrophobic and hydrophilic albumin microspheres and determination of surface carboxylic acid and amine residues. Int J Pharm 151:47–55
Marty JJ, Oppenheimer RC, Speiser P (1978) Nanoparticles—a new colloidal drug delivery system. Pharm Acta Helv 53:17–23
Meloun B, Moravek L, Kostka V (1975) Complete amino acid sequence of human serum albumin. FEBS Lett 58:134–137
Merodio M, Arnedo A, Renedo MJ, Irache JM (2001) Ganciclovir-loaded albumin nanoparticles: characterization and in vitro release properties. Eur J Pharm Sci 12:251–259
Minkowski H (1904) Dichteste gitterförmige Lagerung kongruenter Körper. Nachr Aka Wiss Göttingen Math Phys Kl II:311–355
Moghimi SM, Hunter AC, Murray JC (2001) Long-circulating and target-speci c nanoparticles: theory to practice. Pharmacol Rev 53:283–318
Montisci M-J, Giovannuci G, Duchêne D, Ponchel G (2001) Covalent coupling of asparagus pea and tomato lectins to poly(lactide) microspheres. Int J Pharm 215:153–161
Müller GM, Leuenberger H, Kissel T (1996) Albumin nanospheres as carriers for passive drug targeting: an optimized manufacturing technique. Pharm Res 13:32–37
OECD Joint Meeting of the Chemicals Committee, Working Party on Manufactured Nanomaterials (2008) Series on the safety of manufactured nanomaterials, No. 6. List of manufactured nanomaterials and list of endpoints for phase one of the OECD testing programme. ENV/JM/MONO(2008)13/REV http://www.oecd.org/ehs For updates see http://www.oecd.org/env/nanosafety
Ogan MD, Schmiedl U, Mosely ME, Grodd W, Paajanen H, Brasch RC (1987) Albumin labeled with Gd-DTPA: an intravascular contrast-enhancing agent for magnetic resonance blood pool imaging: preparation and characterization. Invest Radiol 22:665–671
Ostrowsky N, Sornette D, Parker P, Pike ER (1981) Exponential sampling method for light scattering polydispersity analysis. Optica Acta 28:1059–1070
Pallansch MJ, Briggs DR (1954) A study of the interaction of dodecyl sulfate with bovine serum albumin. J Am Chem Soc 76:1396–1403
Parmelee DJ, Walovitch RC, Ouellet HS, Lauffer RB (1997) Preclinical evaluation of the pharmacokinetics, biodistribution, and elimination of MS-325, a blood pool agent for magnetic resonance imaging. Invest Radiol 32:741–747
Paschkunova-Martic I, Kremser C, Mistlberger K, Shcherbakova N, Dietrich H, Talasz H, Zou Y, Hugl B, Galanski M, Stöger E, Pfaller K, Hödiner I, Buchberger W, Keppler B, Debbage P (2005) Design, synthesis, physical and chemical characterization, and biological interactions of lectin-targeted latex nanoparticles bearing Gd-DTPA chelates: an exploration of magnetic resonance molecular imaging (MRMI). Histochem Cell Biol 123:283–301
Peters T Jr (1977) Serum albumin: recent progress in the understanding of its structure and biosynthesis. Clin Chem 23:5–12
Peters T Jr (1985) Serum albumin. Adv Protein Chem 37:161–245
Peters T Jr (1996) All about albumin: biochemistry, genetics and medical applications. Academic Press, San Diego
Peterson HA, Foster JF (1965) The microheterogeneity of plasma albumins, II. Preparation and solubility properties of subfractions. J Biol Chem 240:2503–2507
Port M, Idée J-M, Medina C, Robic C, Sabatou M, Corot C (2008) Ef ciency, thermodynamic and kinetic stability of marketed gadolinium chelates and their possible clinical consequences: a critical review. Biometals 21:469–490
Preda A, van Vliet M, Krestin GP, Brasch RC, van Dijke CF (2006) Magnetic resonance macromolecular agents for monitoring tumor microvessels and angiogenesis inhibition. Invest Radiol 41:325–331
Provencher SW (1979) Inverse problems in polymer characterization: direct analysis of polydispersity with photon correlation spectroscopy. Makromol Chem 180:201–209
Putnam FW (1984) The plasma proteins, vol 4, 2nd edn. Academic Press, London
Quillin ML, Matthews BW (2000) Accurate calculation of the density of proteins. Acta Cryst D56:791–794
Rainey TG, Read CA (1994) The pharmacological approach to the critically ill patient, 3rd edn. Williams & Wilkins, Baltimore, pp 272–290
Reid C (1996) Hilbert. Copernicus Books, New York, 228 p. ISBN 0-387-94674-8
Riess G (2003) Micellization of block copolymers. Prog Polym Sci 28:1107–1170
Rinck PA (2008) Radiologists meet with heavy collateral damage. Diagn Imaging Europe Nov 2008:19–22
Ring J, Messmer K (1977) Incidence and severity of anaphylactoid reactions to colloid volume substitutes. Lancet 1:466–469
Roberts JS, Bratton SL (1998) Colloid volume expanders: problems, pitfalls and possibilities. Drugs 55:621–630
Rofsky NM, Sherry AD, Lenkinski RE (2008) Nephrogenic systemic brosis: a chemical perspective. Radiology 247:608–612
Rowe D, Gray JJ (2000) The Hilbert challenge. Oxford University Press, London, 315 p. ISBN 0-19-850651-1
Sadowski EA, Bennett LK, Chan MR, Wentland AL, Garrett AL, Garrett RW, Djamali A (2007) Nephrogenic systemic brosis: risk factors and incidence estimation. Radiology 243:148–157
Schmiedl U, Ogan M, Paajanen H, Marotti M, Crooks LE, Brito AC, Brasch RC (1987) Albumin labeled with Gd-DTPA as an intravascular, blood pool-enhancing agent for MR imaging: biodistribution and imaging studies. Radiology 162:205–210
Seneterre E, Taourel P, Bouvier Y, Pradel J, Van Beers B, Daures J-P, Pringot J, Mathieu D, Bruel J-M (1996) Detection of hepatic metastases: ferumoxides-enhanced MR imaging versus unenhanced MR imaging and CT during arterial portography. Radiology 200:785–792
Shahbazi-Gahrouei D, Williams M, Allen BJ (2001) Synthesis and application of Gd-porphyrins as MR imaging agent for cancer detection. Iran Biomed J 5:87–95

Shahbazi-Gahrouei D, Roufeh M, Tavakoli MB (2006) Gadolinium-diethylenetriaminepenta-acetic acid conjugated with monoclonal antibody C595 as new magnetic resonance imaging contrast agents for breast cancer (MCF-7) detection. Iran Biomed J 10:209–213

Shapiro MG, Atanasijevic T, Faas H, Westmeyer GG, Gasanoff A (2006) Dynamic imaging with MRI contrast agents: quantitative considerations. Magn Reson Imaging 24:449–462

Singh A, Patel T, Hertel J, Bernardo M, Kausz A, Brenner L (2008) Safety of ferumoxytol in patients with anemia and CKD. Am J Kidney Dis 52:907–915

Sipkins DA, Cheresh DA, Kazemi MR, Nevin LM, Bednarski MD, Li KC (1998) Detection of tumor angiogenesis in vivo by alphaVbeta3-targeted magnetic resonance imaging. Nat Med 4:623–626

Soelder E, Kremser C, Rohr I, Hutzler P, Debbage P (2009) Molecular mapping deep within a living human organ: analysis of microvessel function on the timescale of seconds and with sub-micrometre spatial resolution. Histochem Cell Biol 131:537–551

Soriano I, Llabres M, Evora C (1995) Release control of albumin from polylactic acid microspheres. Int J Pharm 125:223–230

Spector AA (1975) Fatty acid binding to plasma albumin. J Lipid Res 16:165–179

Stehle G, Sinn H, Wunder A, Schrenk HH, Stolz G, Maier-Borst W, Heene DL (1997) The loading rate determines tumor targeting properties of methotrexate-albumin conjugates in rats. Anti-Cancer Drugs 8:677–685

Stewart AJ, Blindauer CA, Berezenko S, Sleep D, Sadler PJ (2003) Interdomain zinc site on human albumin. Proc Natl Acad Sci USA 100:3701–3706

Sugio S, Kashima A, Mochizuki S, Noda M, Kobayashi K (1999) Crystal structure of human serum albumin at 2.5 A resolution. Protein Eng 12:439–446

Tabor E (1999) The epidemiology of virus transmission by plasma derivatives: clinical studies verifying the lack of transmission of hepatitis B and C viruses and HIV type 1. Transfusion 39:1160–1168

The Albumin Reviewers, Alderson P, Bunn F, Li Wan Po A, Li L, Roberts I, Schierhout G (2004) Human albumin solution for resuscitation and volume expansion in critically ill patients. The Cochrane Database of Systematic Reviews 2004, Issue 4. Art. No. CD001208.pub2. doi:10.1002/14651858.CD001208.pub2

Tomlinson E, Burger JJ (1995) Incorporation of water soluble drugs in albumin microspheres. In: Widder KJ, Green R (eds) Part A: drug and enzyme targeting. Methods in enzymology, vol 112, Academic Press, London, pp 27–43

Torchilin VP (2002) PEG-based micelles as carriers of contrast agents for different imaging modalities. Adv Drug Deliv Rev 54:235–252

Torquato S, Jiao Y (2009) Dense packings of the Platonic and Archimedean solids. Nature 460:876–879

Tweedle MF (1992) Physicochemical properties of gadoteridol and other magnetic resonance contrast agents. Invest Radiol 27(Suppl 1):S2–S6

Unger EC, Totty WG, Otsuka FL, Murphy WA, Welch MS, Connett JM, Philpott GW (1985) Magnetic resonance imaging using gadolinium-labeled monoclonal antibody. Invest Radiol 20:693–700

Unger RE, Krump-Konvalinkova V, Peters K, Kirkpatrick CJ (2002) In vitro expression of the endothelial phenotype: comparative study of primary isolated cells and cell lines, including the novel cell line HPMEC-ST1.6R. Microvasc Res 64:384–397

Verrecchia T, Huve P, Bazile D, Veillard M, Spenlehauer G, Couvreur P (1993) Adsorption/desorption of human serum albumin at the surface of poly(lactic acid) nanoparticles prepared by a solvent evaporation process. J Biomed Mater Res 27:1019–1028

Vogel V, Langer K, Balthasar S, Schuck P, Mäle W, Haase W, van den Broek JA, Tziatzios C, Schubert D (2002) Characterization of serum albumin nanoparticles by sedimentation velocity analysis and electron microscopy. Progr Colloid Polym Sci 119:31–36

Weber C, Coester C, Kreuter J, Langer K (2000a) Desolvation process and surface characterisation of protein nanoparticles. Int J Pharm 194:91–102

Weber C, Reiss S, Langer K (2000b) Preparation of surface modi ed protein nanoparticles by introduction of sulfhydryl troups. Int J Pharm 211:67–78

Wedeking P, Kumar K, Tweedle MF (1992) Dissociation of gadolinium chelates in mice: relationship to chemical characteristics. Mag Reson Imaging 10:641–648

Weyl H (1944) David Hilbert and his mathematical work. Bull Am Math Soc 50:612–654

White GW, Gibby WA, Tweedle MF (2006) Comparison of Gd(DTPA-BMA) (Omniscan) versus Gd(HP-DO3A) (ProHance) relative to gadolinium retention in human bone tissue by inductively coupled mass spectroscopy. Invest Radiol 41:272–278

Wilkes MM, Navickis RJ (2001) Patient survival after human albumin administration. A meta-analysis of randomized, controlled trials. Ann Intern Med 135:149–164

Winter PM, Morawski AM, Caruthers SD, Fuhrhop RW, Zhang H, Williams TA, Allen JS, Lacy EK, Robertson JD, Lanza GM, Wickline SA (2003) Molecular Imaging of angiogenesis in early-stage atherosclerosis with $\alpha_v\beta_3$-integrin-targeted nanoparticles. Circulation 108:2270–2274

Yaxley PE (2009) Review of the human albumin controversy. Michigan Veterinary Conference, 22-25.01.2009

Yuan F (1998) Transvascular drug delivery in solid tumors. Semin Radiat Oncol 8:164–175